

**SYNTHESIS AND CHARACTERIZATION OF CERIUM DOPED
COPPER OXIDE NANOPARTICLES BY SOLUTION
COMBUSTION TECHNIQUE**

MASTER OF SCIENCE (M.SC.) IN PHYSICS

by

Md. Saiduzzaman

Student ID: 0417142513F

Session: April, 2017



**DEPARTMENT OF PHYSICS
BANGLADESH UNIVERSITY OF ENGINEERING AND TECHNOLOGY
DHAKA – 1000, BANGLADESH**

November, 2019

**SYNTHESIS AND CHARACTERIZATION OF CERIUM DOPED
COPPER OXIDE NANOPARTICLES BY SOLUTION
COMBUSTION TECHNIQUE**

A dissertation submitted to the Department of Physics, Bangladesh University of Engineering and Technology (BUET), Dhaka in partial fulfillment of the requirements for the degree of

MASTER OF SCIENCE (M.Sc.) IN PHYSICS

by

Md. Saiduzzaman

Student ID: 0417142513F

Session: April, 2017



**DEPARTMENT OF PHYSICS
BANGLADESH UNIVERSITY OF ENGINEERING AND TECHNOLOGY
DHAKA-1000, BANGLADESH**

November, 2019

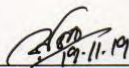
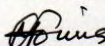
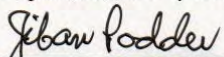
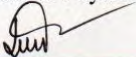
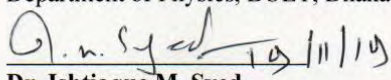
**BANGLADESH UNIVERSITY OF ENGINEERING & TECHNOLOGY (BUET), DHAKA
DEPARTMENT OF PHYSICS**



Certification of Thesis

The thesis titled “**SYNTHESIS AND CHARACTERIZATION OF CERIUM DOPED COPPER OXIDE NANOPARTICLES BY SOLUTION COMBUSTION TECHNIQUE**” submitted by **Md. Saiduzzaman**, Roll No. 0417142513F, Session: April/2017, has been accepted as satisfactory in partial fulfillment of the requirement for the degree of **Masters of Science (M.Sc.)** in Physics on 19 November, 2019.

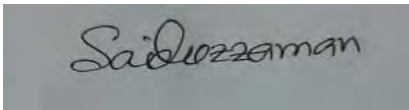
BOARD OF EXAMINERS

 19.11.19	Dr. Muhammad Rakibul Isalm (Supervisor) Assistant Professor Department of Physics, BUET, Dhaka	Chairman
	Dr. Md. Forhad Mina Professor and Head Department of Physics, BUET, Dhaka-1000	Member (Ex-Officio)
	Dr. Jiban Podder Professor Department of Physics, BUET, Dhaka-1000	Member
	Dr. Mohammad Jellur Rahman Associate Professor Department of Physics, BUET, Dhaka-1000	Member
	Dr. Ishtiaque M. Syed Professor Department of Physics University of Dhaka, Dhaka-1000	Member (External)

CANDIDATE'S DECLARATION

It is hereby declared that this thesis or any part of it has not been submitted elsewhere for the award of any degree or diploma.

Signature of the candidate

A rectangular box containing a handwritten signature in black ink. The signature is written in a cursive style and reads "Md. Saiduzzaman".

Md. Saiduzzaman

Student ID: 0417142513F

Session: April, 2017.

Dedicated
To
My Beloved Parents

ACKNOWLEDGEMENT

First of all, I humbly acknowledge my heartfelt gratitude to the almighty Allah, the most gracious, benevolent and merciful whose benediction has been guiding me to the light throughout the days and always.

I wish to express my deepest gratitude and sincere thanks to my honorable supervisor Dr. Muhammad Rakibul Islam, Assistant Professor, Department of Physics, Bangladesh University of Engineering and Technology (BUET), Dhaka-1000, Bangladesh for providing me an opportunity to work under his guidance. His kind attention, care and continuous encouragement have been a source of inspiration for me throughout the research.

I am thankful to Professor Dr. Md. Forhad Mina, Head, Department of Physics, BUET for providing me necessary facilities to carry out this research work. I am also thankful to Professor Dr. Jiban Podder, Professor Dr. A. K. M. Akther Hossain, Dr. Mohammad Jellur Rahman, Mrs. Mehnaz Sharmin and other teachers in the Department of Physics, BUET for inspiration and constructive suggestions.

I am extremely grateful to my others respected teachers of Department of Physics, BUET for their intellectual help and continuous inspiration throughout my research work. I would like to give my cordial thanks to my friends Md. Shaficul Islam Mollik and Md. Golam Azam for their mental and physical help throughout my research period. I would like to give special thanks to my lab mates Md. Mojibul Haque, Bidhan Chandra Dev, Md. Nurul Islam, Md. Jayed Ibn Obayed, Md. Nazmus Sakib Pias for their help and support.

I am also grateful to the authority of Department of Physics, BUET for providing me the logistic supports for this thesis work. Sincere acknowledgement to the Bangladesh University Grants Commission and the Committee for Advanced Studies & Research (CASR), BUET for granting the funds to carry out this research.

At last, I would like to thank and acknowledge my parents whose unlimited love and blissful inspiration were always with me, to lead me to success in my life. I am also thankful to my siblings, family members and relatives for their constant inspiration, support, sacrifices and help to complete the thesis successfully.

Md. Saiduzzaman

November, 2019

ABSTRACT

Recently nanoparticles (NPs) have gained significant research attention due to their unique physical, chemical, mechanical, electrical, optical, catalytic and magnetic properties compared to their bulk counterparts. Abundance in nature, non-toxicity, biocompatibility and easy synthesis mechanism has made Copper Oxide (CuO) one of the most promising NPs. In this study CuO and Ce doped CuO NPs were synthesized by a cost-effective, simple sol-gel auto-combustion process with the doping concentration of Ce varying between 0 to 8 mole%. X-ray Diffraction study was performed to characterize the crystal structure of the CuO and Ce doped CuO NPs. Reitveld analysis was used to reveal the structural information of the NPs. The effect of Ce doping on the different structural parameters such as lattice type, bond length, bond angles and reason behind the change of lattice parameter, strain, and stress was also studied in details. The surface morphology of the NPs was studied by Field Emission Scanning Electron Microscope (FESEM) which shows reduction of the particle size with Ce doping. Fourier Transform Infrared Spectroscopy (FTIR) analysis was performed to study the chemical bonding of the NPs which shows presence of Cu and O bond vibration in the NPs. Raman spectroscopy of the Ce doped CuO NPs shows a change in the intensities and number of modes which are attributed to the presence of intrinsic defects. Optical properties of the NPs were investigated by UV-Visible Spectroscopy. Ce doping was found to reduce the optical band gap of the NPs. It was found the 2 mole% Ce doping reduces the band gap of CuO NPs from 1.72 eV to 1.40 eV. A further increase in Ce dopant enhances the band gap. However it is far less than that pure CuO. Photo-catalytic activity of pure CuO NPs and Ce-doped CuO NPs have been examined by performing the photo degradation of methylene blue (MB) under the visible light irradiation. The Photo-catalytic studies shows that Ce doping improves the photo-catalytic activity of CuO NPs. 2 mole% Ce doped CuO NPs yields the best photo-catalytic activity and the activity reduces with the increase of dopant concentration. The higher surface area of the NPs due to smaller particle size distribution together with its lower band gap is responsible for the enhanced photo-catalytic activity of Ce doped CuO NPs than the pure CuO NPs. The Ce doped CuO NPs synthesized by an effective and economic route may open up a versatile route to enhance the photo-catalytic activity of CuO NPs and can find their applications in water purification and environment cleaning.

CONTENTS

	Page no.
ACKNOWLEDGEMENT	iv
ABSTRACT	v
INDEX	vi
LIST OF FIGURE	ix
LIST OF TABLES	xi
LIST OF ABBREVIATIONS	xi

INDEX

CHAPTER 1 INTRODUCTION

1.1 Introduction	1
1.2. Motivation and Background of the Study	2
1.3. Statement of the Problem	4
1.4. Objectives of the Study	4
1.5. Organization of the Thesis	5

CHAPTER 2 THEORETICAL BACKGROUND

2.1 Nanoscience and Nanotechnology	6
2.1 Nanomaterials	7
2.3 Properties of Nanomaterials	7
2.4 Classifications of Nanomaterials	8
2.5 Nanoparticles (NPs)	10
2.6 Properties of Cu ₂ O	11
2.7 Properties of CuO	11
2.8 Synthesis of NPs	12
2.8.1 Top-down methods	12
2.8.2 Bottom-up methods	13

2.9	Some Other Methods for Preparing Nanomaterials	13
2.9.1	Hydrothermal method	13
2.9.2	Gas phase method	14
2.9.3	Microwave synthesis	14
2.10	Sol-gel Auto-combustion Method	14
2.10.1	Auto generation of combustion technique in sol-gel method	15
2.11.	Photo-catalytic Activity	16
2.11.1	Photo-catalytic mechanism	17
2.11.2	Description of oxidation mechanism	18
2.11.3	Description of reduction mechanism	19
2.11.4	Operating and affecting parameters of photo-catalysis	20
2.11.4.1	Crystal structure, shape, size and surface area of catalyst	20
2.12	Characterization Techniques	21
2.12.1	X-Ray Diffraction (XRD)	21
2.12.1.1	Principle	21
2.12.1.2	Bragg's law	21
2.12.1.3	XRD setup	23
2.12.2	Field Emission Scanning Electron Microscope (FESEM)	24
2.12.2.1	Principle	25
2.12.3	Fourier Transform Infrared Spectrometer (FTIR)	27
2.12.3.1	FTIR peak analysis	29
2.12.4	UV-Visible Spectroscopy	31

CHAPTER 3

EXPERIMENTAL METHODS AND CHARACTERIZATION TECHNIQUES

3.1	Precursors	32
3.2	Synthesis of CuO and Ce Doped CuO NPs	32
3.2.1	Experimental setup	32
3.2.2	Synthesis of pure CuO NPs	33
3.2.2.1	Conditions	33
3.3	Synthesis of Ce Doped CuO NPs	35

3.3.1	Required chemicals	35
3.4	XRD Experimental Setup	35
3.5	Field Emission Scanning Electron Spectroscopy setup	36
3.6	UV-Visible Experimental Setup	36
3.7	FTIR Setup	37
3.8	Photo-catalysis Activity Experimental Setup	37

CHAPTER 4

RESULTS AND DISCUSSION

4.1	Sample Preparation Procedure for Characterization	38
4.2	Field Emission Scanning Electron Microscopy (FESEM)	38
4.3	EDS Analysis	40
4.3.1	Atom (%), mass (%), material presents in the samples	41
4.4	X-Ray Diffraction (XRD)	41
4.4.1	Reitvelt analysis of pure CuO NPs	42
4.4.2	3D structure of Ce doped CuO NPs	44
4.4.3	Reitvelt analysis of Ce NPs on CuO NPs	45
4.4.4	XRD spectra of pure CuO and Ce doped CuO NPs	46
4.4.5	Change of bond angle, bond length	50
4.4.6	Determination of particle size	53
4.5	FTIR Analysis	55
4.6	Raman Spectrum	57
4.7	UV-Vis Characteristics	59
4.7.1	Absorbance spectra of pure CuO and Ce doped CuO NPs	59
4.7.2	Band gap of pure CuO and Ce doped CuO NPs	60
4.7.3	Variation of optical band gap due to Ce doping	61
4.8	Photo-catalytic Activity of CuO and Ce Doped CuO NPs	62
4.8.1	Photo-catalytic mechanism	65

CHAPTER 5

SUMMARY AND CONCLUSION

5.1 Conclusion	68
5.2 Future Work	69

CHAPTER 6

REFERENCES

References	70
------------	----

LIST OF FIGURES

Figure 1: Classification of nanomaterials according to their dimension.	9
Figure 2: Structural information of CuO NPs.	11
Figure 3: Schematic variety of nanostructure synthesis and assembly approaches.	12
Figure 4: Schematic representation of semiconductor photo-catalytic mechanism	18
Figure 5: Schematic representation of oxidation mechanism	19
Figure 6: Schematic representation of reduction mechanism	19
Figure 7: A philips pw 3040 X'Pert Pro X-ray diffractometer	21
Figure 8: Bragg's diffraction pattern	22
Figure 9: A simple diagram of optics used in the XRD instrument.	23
Figure 10: Schematic diagram of FESEM	25
Figure 11: A Photo of FESEM JSM-7600F	27
Figure 12: Schematic illustration of an FTIR system	28
Figure 13: Schematic diagram of UV-Visible spectrometer	31
Figure 14: Experimental setup for the preparation of CuO and Ce doped CuO NPs.	32
Figure 15: Synthesis process of CuO NPs	34
Figure 16: Schematic diagram of preparation of CuO NPs.	34
Figure 17: Instrumental setup for XRD measurement.	35
Figure 18: FESEM setup for taking images of NPs	36
Figure 19: UV-Vis experimental setup	36
Figure 20: FTIR setup for experimental setup.	37
Figure 21: Homemade photo-catalytic chamber	37
Figure 22: FESEM images of (a) pure CuO NPs, (b) 2 mole% Ce (c) 4 mole% Ce (d) 6 mole% Ce and (e) 8 mole% Ce doped CuO NPs.	39
Figure 23: EDS spectra of (a) pure CuO NPs, (b) 2 mole% Ce (c) 4 mole% Ce (d) 6	

mole% Ce and (e) 8 mole% Ce doped CuO NPs.	40
Figure 24: Reitvelt analysis of (a) pure CuO NPs, (b) 2 mole% Ce, (c) 4 mole% Ce, (d) 6 mole% Ce and (e) 8 mole% Ce doped CuO NPs.	43
Figure 25: Crystal structure of (a) pure CuO NPs, (b) 2 mole% Ce, (c) 4 mole% Ce, (d) 6 mole% Ce and (e) 8 mole% Ce doped CuO NPs obtained by Reitvelt analysis.	44
Figure 26: Intensity distribution of Pure CuO and Ce doped CuO NPs.	46
Figure 27: Magnification of XRD pattern of (-111) plane	47
Figure 28: Variation of peak position due to Ce doping on CuO NPs.	48
Figure 29: (a) Change of FWHM of (-111) plane, (b) change of d-spacing, (c) change of micro strength due to Ce doping on CuO NPs.	49
Figure 30: Variation of bond length of Cu-O (left) and Cu-O (right) of the prepared NPs	51
Figure 31: Cu-O bond length (\AA) (red line) and Cu-Cu atomic distance (\AA) variation (black line) due to addition of Ce on CuO NPs.	52
Figure 32: Variation of bond angle due to Ce doping on CuO NPs.	52
Figure 33: O-Cu-O bond angle	52
Figure 34: Particle size variation pure and Ce doped CuO NPs	54
Figure 35: FTIR spectra of pure CuO and Ce doped CuO NPs	55
Figure 36: Raman spectra of pure and Ce doped CuO NPs.	58
Figure 37: Absorbance spectra of pure CuO and Ce doped CuO NPs.	60
Figure 38: Variation of energy gap due to doping of Ce NPs in pure CuO NPs	61
Figure 39: The variation in UV-Visible absorption spectra of methylene blue (MB) dye solution as a function of irradiation time in the presence of (a) pure CuO NPs, (b) 2 mole% Ce, (c) 4 mole% Ce, (d) 6 mole% Ce and (e) 8 mole% Ce doped CuO NPs as a catalyst under Visible light illumination.	63
Figure 40: Degradation percentage of MB dye for pure and Ce doped NPs	64
Figure 41: Degradation rate of MB dye for pure and Ce doped CuO NPs	64
Figure 42: Degradation percentage for first 30 minute of MB dye for pure and Ce doped CuO NPs	65
Figure 43: Color change of the MB dye with prepared NPs under Visible light irradiation	65
Figure 44: Equation of photo-catalytic mechanism	66
Figure 45: Photo-catalytic mechanism	66

LIST OF TABLES

Table 1: Classification of nanomaterials based on dimension	9
Table 2: Required chemicals for preparing pure and Ce doped CuO NPs.	35
Table 3: Material presence, Atom (%) and mass (%) of the pure CuO and Ce doped CuO NPs samples.	41
Table 4: Bond length and bond angle for CuO and Ce doped CuO NPs.	51
Table 5: Change of particle size as a result of Ce doping on CuO NPs.	53
Table 6: Change of band gap as a result of Ce doping on CuO NPs.	60

LIST OF ABBREVIATIONS

SYMBOL	ABBREVIATION
1D	One Dimensional
2D	Two Dimensional
3D	Three Dimensional
D	Crystallite size
d	Average particle size
CuO	Cupric Oxide
Cu ₂ O	Cuprus Oxide
Ce	Cerium
CeO ₂	Cerium Oxide
DW	Distill Water
DDW	Double Distill Water
DI	De-ionized
EDS	Energy Dispersive Spectroscopy
FESEM	Field Emission Scanning Electron Microscope
FTIR	Fourier Transform Infrared Spectroscopy
NPs	Nanoparticles
TEM	Transmission Electron Microscopy
XRD	X-ray Diffraction
MB	Methylene Blue

CHAPTER 1

INTRODUCTION

1.1 Introduction

Nanotechnology is the science and technology of very small things in particular, things that are less than 100 nanometers in size. The area of nanoscience and nanotechnology has become increasing importance in recent years and a wide variety of applications of these materials are expected in various branches of science and technology comprising Physics, Chemistry, Biology, Materials Science, Medicine, Computational Science, Environmental Science etc. and thus providing a profound impact in our daily lives [1-3].

Nanoparticles (NPs) have become the core material in nanotechnology owing to their unique physical, chemical, mechanical, electrical, optical, catalytic and magnetic properties compared to their bulk counterparts [1]. In general, these properties depend upon the size and shape of the particles [2, 3]. NPs have wide range of applications in various fields like medicine, pharmaceuticals, biotechnology, information technology, optical and biological sensors, photovoltaic cells, agriculture, conductive materials, coating formulation etc.

Copper oxide stands as the most significant materials for being the most current transition metal in the lithosphere. Copper oxide is abundantly found in nature. Copper oxide is prevalent, inexpensive and the most widely used bio-compatible material which plays an imperative role in many biological and technological processes [10]. The two most common forms of copper oxides in nature are Cuprous oxide (Cu_2O) and Cupric oxide (CuO) which are also very important in the field of scientific research [11]. Copper oxide NPs has gained significant attention due to their non-toxicity, bio-compatibility, magnetic properties and large surface area to volume ratio as well as good reactive surface [5]. The extreme reactivity of Copper makes it difficult to study and problematic for applications. However, magnetic and catalytic properties have diverted the attention toward Copper's potential. Synthesis methods, crystallization, size, shape, and quality of the Copper oxide NPs greatly affect these behaviors. The shapes of nano materials also exert tremendous impact on their properties, more importantly in catalysis [7]. Shape change shows crystal facets, and the atomic

arrangements in each fact have reflective effects on its properties [8]. The development of protocols for desired morphology, size, and shape is under consideration [9].

Several methods are being adapted for the synthesis of Copper oxide NPs, which include sol-gel process [13], solid state reaction [20], co-precipitation [14], sono-chemical method [15], hydrothermal techniques [16], microwave irradiation [21, 22], non-aqueous synthesis [17], plasma [23] and thermal decomposition method [25], ultrasound irradiation [18], micro-emulsion method [19] etc. All these methods require high pressures and temperatures, even involving harmful chemicals. In contrast, the above method solution combustion method is a versatile, simple, rapid and single steps process which involves a self-sustained reaction in homogeneous solution of different oxidizers and fuels. Developing a facile and cost-effective method for synthesizing copper oxide NPs is importance and still a challenge for materials scientists. Utilization of nontoxic chemicals, environmentally benign solvents, and inexpensive materials are some of the key issues that merit important consideration in this synthetic strategy.

1.2 Motivation and Background of the Study

The unprecedented physicochemical properties of engineered nano materials are attributable to their small size (surface area and size distribution), chemical composition (purity, crystallinity, electronic properties etc.), surface structure (surface reactivity, surface groups, inorganic or organic coatings etc.), solubility, shape and aggregation. Studies have shown that the size, morphology, stability and properties (chemical and physical) of the metal NPs are strongly influenced by the conditions of experiment, the kinetics of interaction of metal ions with reducing agents and the adsorption processes of stabilizing agent with metal NPs [27]. Due to the exclusive properties like magnetic, reactive surface, bio-degradability, bio-compatibility, non-toxicity, high saturation magnetization and low Curie temperature. Copper oxide has wide variety of applications such as gas sensors, batteries, magnetic storage media, solar energy transformation, electronics, semiconductors, field emission and catalysis [26]. It is also utilized as photo thermal active and photo conductive compound. The increase comprehensive strength, thermal properties and microstructure of self-compacting concrete with CuO NPs were investigated [29]. The CuO NPs gave very high activity for detection of H_2O_2 [4]. It is also used as an electrochemical pH sensor [5]. The photocatalytic evolution of H_2O_2 under simulated sunlight irradiation using CuO was studied

[6]. A recyclable catalyst for oxidative phenol coupling reaction was made with CuO NPs [7]. Therefore, exponential growth in research focuses on synthesis, properties and applications of CuO NPs that have been accomplished in recent years.

The presence of both organic and inorganic pollutants in water due to industrial, agricultural, and domestic activities has led to the global need for the development of new, improved, and advanced but effective technologies to effectively address the challenges of water quality. It is therefore necessary to develop a technology which would completely remove contaminants from contaminated waters. In this purpose we need such a material that removes dye from the water in presence of visible light. So I motivated to explore a catalyst particle which is treated as water treatment.

Synthesis of NPs with the required quality and desired properties is one of the important issues in competitive nanotechnology. The development of easy and cost-effective processes for the synthesis of NPs is evolving into an important branch of nanotechnology. In combustion synthesis of NPs involves three main steps, including: (a) selection of solvent medium, (b) selection of nitrate compound of Copper and (c) selection of fuel substances for the NPs synthesis [28]. As a consequence, in order to meet the exponentially growing technological demand, it is desirable to study the inexpensive synthesis route for the synthesis of various NPs and presently available literature reveals that the CuO NPs synthesis by combustion technique has been unexplored and underexploited [29].

Hence developing of a cost effective and environment friendly approach has added much importance because of its eco-friendly products, biocompatibility and economic viability in the long run. The eco-friendly and green chemistry perspective for the NPs synthesis are the choice of the solvent medium, reducing agent and non-toxic material respectively for the stabilization of NPs [34]. Among the various particle synthetic methods, the raw materials which are used in the combustion process are available, safe to handle and possess a broad viability of metabolites [30].

In succession of the efforts for synthesizing of stable and biocompatible CuO NPs here we report a facile, less labor and biodegradable synthesis using the water solvent and cheap organic material, citric acid as fuel which has been chosen due to the availability in our country.

1.3. Statement of the Problem

CuO having semiconductor nanostructure is attractive component to be used for nanometric scale electronic and photonic device applications because of their unique chemical and physical properties. However, there are still significant challenges that have to be overcome in order to produce efficient CuO devices.

The first challenge is in understanding the structural property of CuO and Ce doped CuO NPs. Another main obstacle for the commercialization of CuO based homojunction devices is the absence of stable and reproducible p-type doping with high hole concentrations and large carrier mobility. As a consequence, n-doping of CuO is still an unsolved problem. It is widely acknowledged that the morphology of CuO nanostructures is highly sensitive. It may form either CuO or Cu₂O as it has two stable oxide formations. As a result, it is difficult to make specific copper oxide NPs. Besides Ce is a reactive NPs, it can use for explosives, missiles can be used in combustion process without Oxygen. It is a very hard to keep it a stable form. We seek a way to dope a limited but controlled amount of Ce NPs on CuO NPs. We have to aware of toxicity of Ce NPs also. Moreover, it is a challenging task to dope desired amount of Ce NPs properly.

Again, some of the basic properties of CuO are not well understood and are still debatable owing to the different intrinsic defects such as oxygen interstitials (O_i), copper interstitials (Cu_i), oxygen vacancies (V_o), copper vacancies (V_{cu}). Ce was doped on CuO NPs. As a result, all those interstitial position changes. Structural property may change or not. This property changes are studied here. Therefore, the major problem this thesis seeks to address is how to tune the structural, optical, chemical property of CuO and Ce doped CuO NPs.

1.4. Objectives of the Study

The objectives of this study are:

- To synthesize CuO and Ce doped CuO NPs by sol-gel auto-combustion method.
- Study the surface morphology of CuO and Ce doped CuO NPs using Field Emission Scanning Electron Microscopy (FESEM).
- To determine the chemical composition of the samples by Energy Dispersive X-Ray Spectroscopy (EDS).
- Determining the crystal structure and particle size with X-Ray Diffraction (XRD).

- Determining the lattice parameters, micro-strain, micro-stress and texture coefficient of the prepared sample from XRD.
- Studying the effect of Ce-dopant on the different structural parameters of the NPs.
- Study the optical properties and determine the band gap of the CuO and Ce doped CuO NPs by UV-Vis Spectrophotometer.
- To understand the chemical bond of the prepared pure and Ce doped CuO NPs by FTIR.
- To investigate the vibrational mode of the prepared pure and Ce doped CuO NPs by Raman Spectroscopy.
- Investigation of Photo-catalytic of CuO NPs and the role of Ce dopant for the Photo-catalytic properties in the CuO NPs.

1.5. Organization of the Thesis

The thesis consists of five 6 chapters.

Chapter 1st begins with the overview of research background, aims of study and statement of problem.

Chapter 2 provides the introduction of the CuO and the underlying theories and fundamental properties of CuO. The different characterization techniques of CuO are also briefly discussed in this chapter.

Chapter 3 gives a brief description of the experimental equipment, environmental and atmospheric requirements, techniques used to design, synthesize and characterize CuO. The sol-gel auto-combustion method used to synthesize the NPs is discussed in detail.

Chapter 4 reports the results obtained from the characterization and the founded result is discussed there.

Chapter 5 gives the conclusion of the thesis and suggestible works to be done in the future.

Chapter 6 related references of my work.

CHAPTER 2

THEORETICAL BACKGROUND

2.1 Nanoscience and Nanotechnology

The word “Nano” is originated from a Greek word whose meaning is extremely small or dwarfs [31]. The basic concepts behind nanoscience and nanotechnology was reported with a talk entitled “There’s a Plenty of Room at the Bottom” by the Physicist Richard Feynman at the California Institute of Technology on December 29, 1959 [32]. The term “Nanotechnology” was later coined by Professor Norio Taniguchi using Feynman’s explorations of ultra-precision machining. A brief and general definition of nanotechnology by the US National Science and Technology Council [33] states: “The essence of nanotechnology has the capability to work at the molecular level such as atom by atom for the creation of large structures with essentially innovative molecular organization. The aim is to exploit these properties by gaining control of structures and devices at atomic, molecular, and supra molecular levels and to become skilled at well-organized manufacture and use these devices”. The United States National Science Foundation [34] defines nanoscience or nanotechnology is the study which deals with materials and systems deserving the following two key properties:

- The dimension must be at least one dimension from 1-100 nm.

- According to the building block property, larger structures form by the combination of smaller one. According to the microbiological study, the nanoscience leads to the sizes of different types of bio-particles which deals with bacteria, viruses, enzymes etc. fall within the nanometer range.

- The process can be designed with various methodologies which show elementary control over the physical and chemical properties of structures that can be measure by the molecular-scale.

Nanotechnology has the capability at atomic precision which is useful for making of materials, various instruments and systems [34, 35]. Nanotechnology can also be defined as the study and investigation about the synthesis, characterization, exploration and application of nano sized materials which is of 1-100 nm in size and will be valuable and functional for the development of science. A recent advance in the emerging field

of nanotechnology has the capability for the preparation of the highly ordered NPs of various different size and shape which led to the development of the modern technology [36]. The prefix nano means a factor of one billionth (10^{-9}) and can be applied, e.g., to time (nanosecond), volume (nanoliter) weight (nanogram) or length (nanometer or nm).

2.2 Nanomaterials

Nanomaterials made of metals, semiconductors, or oxides are of particular interest for their mechanical, electrical, magnetic, optical, chemical and other properties [37]. Nanomaterials are effectively a bridge between bulk materials and atomic or molecular structures. A bulk material should have constant physical properties regardless of its size but at the nano-scale this is often not the case. For example, the bending of bulk copper (wire, ribbon etc.) occurs with movement of copper atoms/clusters at about the 50 nm scale. Copper NPs smaller than 50 nm are considered super hard materials that do not exhibit the same malleability and ductility as bulk copper [38]. A material such as gold, which is chemically inert at normal scales, can serve as a potent chemical catalyst at nanoscales. Much of the fascination with nanotechnology stems from these quantum and surface phenomena that matter exhibits at the nanoscale.

2.3 Properties of Nanomaterials

The unique properties of various types of intentionally produced nanomaterials give them novel electrical, catalytic, magnetic, mechanical, thermal or imaging features that are highly desirable for applications in commercial, medical, military and environmental sectors [39]. The material properties of nanostructures are different from the bulk due to the high surface area over volume ratio and possible appearance of quantum effects at the nanoscale. As a particle decreases in size, a greater proportion of atoms are found at the surface compared to those inside [40].

For example, a particle of size 30 nm has 5% of its atoms on its surface, at 10 nm 15% of its atoms and at 3 nm 50% of its atoms. Thus, NPs have a much greater surface area per unit mass compared with larger particles. As growth and catalytic chemical reactions occur at surfaces, this means that a given mass of material in nanoparticulate form will be much more reactive than the same mass of material made up of larger particles. In tandem with surface-area effects, quantum effects can begin to dominate

the properties of matter as size is reduced to the nanoscale. These can affect the optical, electrical and magnetic behavior of materials, particularly as the structure or particle size approaches the smaller end of the nanoscale. The large surface area to volume ratio results in a substantial proportion of atoms having different magnetic coupling with neighboring atoms leading to differing magnetic properties. For instance, bulk gold and platinum are non-magnetic but at the nano-size they act as magnetic particles. Gold NPs become ferromagnetic when they are capped with the appropriate molecules. Semiconductors and many metals show large changes in optical properties such as color, as a function of particle size [41]. Colloidal suspensions of gold NPs have a deep red color which becomes progressively more yellow as the particle size increases.

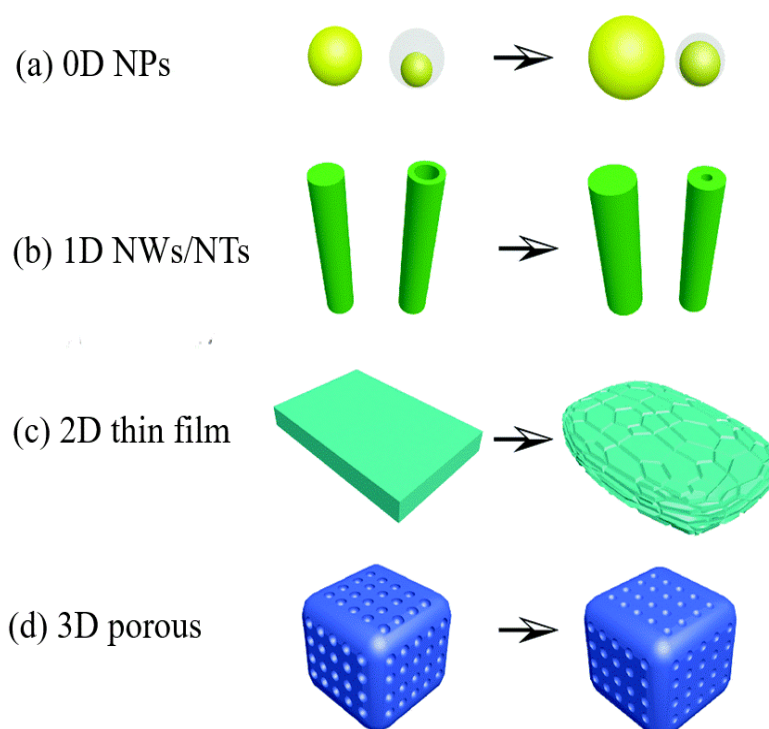
2.4 Classification of Nanomaterials

Generally, nanomaterials are referred as the infrastructure or building blocks element for nanotechnology. The “Building blocks” for nanomaterials consist of carbon-based components and organics, semiconductors, metals and metal oxides [42]. Nanomaterials with structural features at the nanoscale can be found in the form of clusters, thin films, multilayer and nanocrystalline materials which are often expressed by the dimensionality of 0, 1, 2 and 3 as shown in Table 1. The materials include metals, amorphous and crystalline alloys, semiconductors, oxides, nitride and carbide ceramics in the form of clusters, thin films, multilayer and the bulk nanocrystalline materials. Classification of various nanomaterials is shown in Fig. 1.

The familiar nanomaterial ‘carbon black’ was used in industrial production over a century ago. The other early nanomaterials are fumed silica, a form of silicon dioxide (SiO_2), Fe_3O_4 and zinc oxide (ZnO). Nanomaterials can have different properties at nanoscale which is also established by the quantum effects. Among all nanomaterials, some are having better conductivity towards heat and electricity, different magnetic properties, light reflection and also change colors according to their size which is also changed. These properties are a little bit different from the bulk materials. Nanomaterials also have larger surface areas than similar volumes of larger-scale

Table 1: Classification of nanomaterials based on dimension

Dimension	Example of nanomaterials
0D	Nanoparticles, colloids, nanodots, nanoclusters
1D	Nanowires, nanotubes, nanobelts, nanorods
2D	Quantum wells, super lattice, membranes
3D	Nanocomposites, cellular materials, nanocrystal array, block polymers

**Fig. 1: Classification of nanomaterials according to their dimension**

materials which signify the meaning of more surfaces is available for interactions with other materials around them. Nanomaterials are being controlled to nano crystalline size which is less than 100 nm which can show atom-like behaviors. This results from its higher surface energy due to their large surface area and wider band gap between

valence and conduction band. It occurs when they are divided to near atomic size [38, 42]. Nanomaterials are also referred as “a wonder of modern medicine”. It signifies the importance of antibiotics which kill at least six different disease-causing organisms whether the nanomaterials can kill at least 650 cells [43]. Nanomaterials are being enthusiastically researched for specific function like microbial growth inhibition, carriers of antibiotics and also act as killing agents [44].

2.5 Nanoparticles (NPs)

NPs are particles between 1 and 100 nm in size with a surrounding interfacial layer. The interfacial layer is an integral part of nanoscale matter, fundamentally affecting all of its properties. In nanotechnology, a particle is defined as a small object that behaves as a whole unit with respect to its transport and properties. There are two different types of NPs, inorganic NPs and organic NPs. The inorganic NPs include metal and metal oxides, which are potent antibacterial agents. Metal oxide NPs such as silver (Ag), iron oxide (Fe_3O_4), titanium oxide (TiO_2), copper oxide (CuO), and zinc oxide (ZnO) are certain examples of inorganic NPs. Organic NPs include quaternary ammonium compounds, cationic quaternary polyelectrolytes, N-halimane compounds, and chitosan. Organic NPs are generally less stable at high temperatures. Due this reason, inorganic NPs are more preferred as antimicrobial polymers [45].

We are going to introduce here the two main copper oxides, Cu_2O and CuO. Knowledge of the physical properties of these materials, and especially of the surface structure is relevant background when trying to understand the formation and growth of the copper oxide. Then we will discuss the procedure of synthesizing copper oxide NPs and some characteristic techniques.

The most common forms of the oxide (shown in Fig-2) are cupric oxide (CuO) or cuprous oxide (Cu_2O), the principal oxide at low temperature and pressure, and tenorite (or cupric oxide, CuO), dominant at high temperatures and pressures. Another copper oxide structure, paramelaconite (Cu_4O_3), exists as a rare mineral found in hydrothermal deposits of copper. Cuprite has long been known to be the primary oxide for copper at ambient conditions and there is considerable interest in its application to catalysis, optoelectronics and gas sensing and therefore a large amount of work has been done to

determine its physical and chemical characteristics. Tenorite has been studied less and still relatively little is understood about the structure of its surfaces.

2.6 Properties of Cu_2O

Cuprous oxide is a cubic crystalline solid, where copper has a Cu^{1+} oxidation state. It is a p-type semiconductor with a direct band gap of 2.02-2.17 eV (bulk) and an optical gap of 2.62eV (bulk) where optical band gap is 3.6eV (NPs) [46]. It is a promising material for a variety of industrial applications because of its band gap and because it shows negative thermal expansion.

2.7 Properties of CuO

In CuO , the copper atom has oxidation state Cu^{2+} . The unit cell has monoclinic symmetry. It contains four CuO dimers in the crystallographic unit cell and two CuO units in the primitive cell. Each copper atom is located in the center of an oxygen parallelogram [46].

A detailed schematic arrangement of atoms in the conventional unit cell is shown in the following figure:

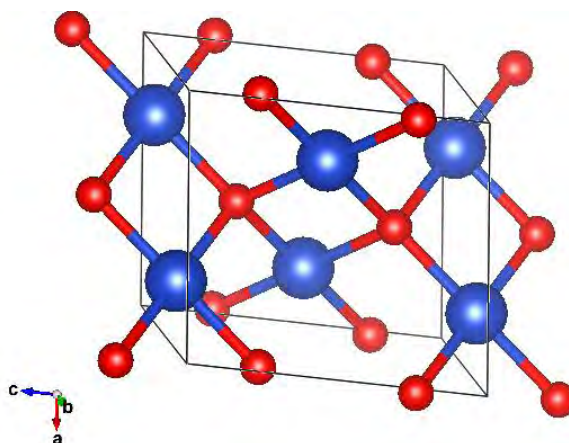


Fig. 2: Structural information of CuO NPs

From fig. 2 it is clearly seen that every atom of one kind (e.g. Cu) is surrounded by four atoms of the other kind (O), or vice versa, which are positioned at the edges of a tetrahedron. This tetrahedral coordination is typical of sp^3 covalent bonding. In a tenorite (CuO) lattice, there are lattice parameters a , b and c , and the internal parameter

and bond angles α , β and γ . The lattice constants of the CuO unit cell are $a=4.68 \text{ \AA}$, $b=3.42 \text{ \AA}$ and $c = 5.12 \text{ \AA}$ and $\alpha=90^\circ$, $\beta=99^\circ$, $\gamma=90^\circ$ [1, 2].

2.8 Synthesis of NPs

NPs fabrication methods can be classified into two approaches. They are (1) Top down and (2) bottom up approach. In the bottom-up approach, smaller components of atomic or molecular dimensions self-assemble together according to a natural physical principle or an externally applied driving force. Top down process starts from large species and subsequently uses finer and finer tools for creating correspondingly smaller structures [3].

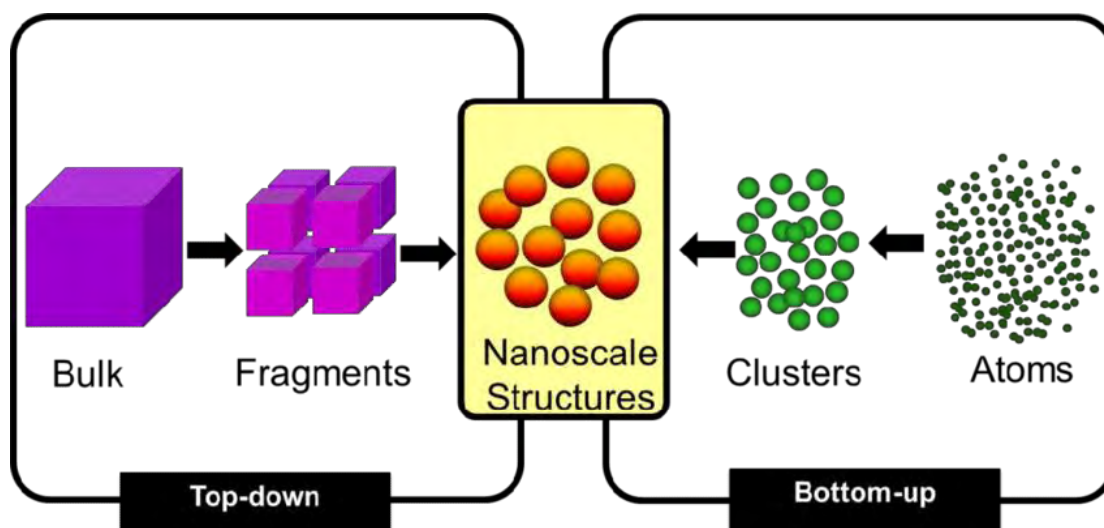


Fig. 3: Schematic variety of nanostructure synthesis and assembly approaches.

2.8.1 Top-down methods

Mechanical-synthetic methods: Mechanical method offers the least expensive ways to produce nanomaterials from bulk materials. Ball milling procedure can produce nanomaterials by mechanical attrition. In this process, kinetic energy from a grinding medium is transferred to a material undergoing reduction.

Compaction and consolidation: In this process, nanomaterials are "put back together" to form materials with enhanced properties. This process can be used to make metallic alloys.

Thermal methods: This method forms a nebulous category.

Electro-spinning method: Nano-thread materials can be produced using this method.

Arc discharge method: This method was first used for making carbon nanotubes.

Plasma methods: Plasmas are created in high-energy situations. The problem with this and other high-energy methods is upscale potential.

Top-down chemical fabrication methods are always easy to upscale and many, such as anodizing, are widespread industrial processes. Top-down methods capable of producing for the most part micron-sized features, although they require energy intensive and expensive materials and facilities.

2.8.2 Bottom-up methods:

Bottom-up methods start with atoms or molecules to form nanomaterials.

Chemical vapor deposition: It is a gas-phase process in which reactive constituents react over a catalyst or pre-templated surface to form nanostructure materials. Precursors in the form of methane or acetylene or other carbon source gases are passed over Co, Fe or Ni catalyst. Once decomposed into carbon, nanotubes are formed by the catalyst particle.

Atomic layer deposition: It is an industrial process. This process is capable of coating any material, regardless of size, with a monolayer or more of a thin film.

Liquid phase methods: This method is within the liquid phase that all of self-assembly and synthesis occurs. Liquid phase methods are up-scalable and cost is low.

Electro-deposition and **electro-less deposition** are very simple ways to make nanomaterials (dots, clusters, colloids, rods, wires, thin films). Many of the new methods are both inexpensive and offer high throughput.

2.9 Some Other Methods for Preparing Nanomaterials

2.9.1 Hydrothermal method

Hydrothermal synthesis is typically carried out in a pressurized vessel called an autoclave with the reaction in aqueous solution [47]. The temperature in the autoclave can be raised above the boiling point of water, reaching the pressure of vapor saturation. This method can be useful to control grain size, particle morphology, crystalline phase and surface chemistry through regulation of the solution composition, reaction temperature, pressure, solvent properties, additives and aging time [48].

2.9.2 Gas phase method

Gas phase methods are ideal for the production of thin films. Chemical vapor deposition (CVD) is a widely used industrial technique that can coat large areas in a short space of time. During the procedure, metal oxide is formed from a chemical reaction or decomposition of a precursor in the gas phase [49]. Physical vapor deposition (PVD) is another thin film deposition technique. The process is similar to chemical vapor deposition (CVD) except that the raw materials/precursors.

2.9.3 Microwave synthesis

Microwave synthesis is relatively new and an interesting technique for the synthesis of oxide materials [50]. Various nanomaterials have been synthesized in remarkably short time under microwave irradiation [51]. Microwave techniques eliminate the use of high temperature calcination for extended periods of time and allow for fast, reproducible synthesis of crystalline metal oxide nanomaterials. Utilizing microwave energy for the thermal treatment generally leads to a very fine particle in the nanocrystalline regime because of the shorter synthesis time and a highly focused local heating.

In the present work, we will synthesize nanoparticles with the sol-gel auto-combustion method, so sol-gel auto-combustion method has been studied briefly as below.

2.10 Sol-gel Auto-combustion Method

2.10.1 Sol-gel method

The sol-gel process is a versatile soft chemical process widely used for synthesizing metal oxides, ceramic and glass materials. The ceramic and glass materials can be obtained in a wide variety of forms: ultra-fine or spherical shaped powders, thin film coatings, ceramic fibers, microporous inorganic membranes.

Sol-gel method normally involves the use of metal alkoxides or organometallic inorganic salts as precursors [64]. In this process, the precursors undergo a series of hydrolysis and poly-condensation reaction to form a colloidal suspension or a sol. The sol-gel process involves the transition of a system from a liquid “sol” (mostly colloidal) into a solid “gel” phase. Then drying of the gel followed by calcination at different temperatures to obtain the metal oxide nanopowder. In sol-gel method it is possible to control the shape, morphology and textual properties of the final materials. In contrast

to high-temperature processes, Sol-gel method has large advantages such as possibility of obtaining metastable materials, achieving superior purity and compositional homogeneity of the products at moderate temperature. Furthermore, this process also influences the particle morphology during the chemical transformation of the molecular precursor to the final oxidic network.

This technique offers many advantages including the low processing temperature, the ability to control the composition on molecular scale and the porosity to obtain high surface area [52] materials, the homogeneity of the final product up to atomic scale. Moreover, it is possible to synthesize complex composition materials, to form higher purity products through the use of high purity reagents. The sol-gel process allows obtaining high quality films up to micron thickness, difficult to obtain using the physical deposition techniques. Moreover, it is possible to synthesize complex composition materials and to provide coatings over complex geometries [53].

2.10.2 Combustion technique

In principle, this synthesis method exploits the energy resulting from the self-propagating highly exothermic redox reaction that occurs during heating metal nitrates (oxidizers) and various organic compounds or fuels (reducing agents). The ignition of the combustion reaction is achieved by rapidly heating the mixture of raw materials at relatively low temperatures usually below 500 °C [54-56].

At the same time, when synthesis conditions are properly selected, the temperature reached in the reaction system (1500 °C) is high enough to facilitate the formation of the desired compound without any other heat treatment. It should be noted that the whole process takes a few seconds only and the reaction byproducts (N₂, H₂O and CO₂) are compatible with the environment. All these remarkable advantages determined material scientists to use more and more frequently combustion synthesis for the preparation of a wide range of materials [57-59].

Unlike many of the synthesis methods, which require an annealing step in order to obtain the desired crystalline compound, combustion synthesis has several advantages:

- It doesn't require annealing
- It is time and energy efficient and last but not least
- It is environmentally friendly.

An additional advantage is that powder characteristics (surface area, crystallite size and grain size) prepared by combustion synthesis can be properly adjusted by changing the synthesis conditions [60].

2.10.3 Auto generation of combustion technique in sol-gel method

In our experiment both techniques combination was used. Combustion process can be auto generated in Sol-gel techniques when gel is formed. Full procedure can be written as below:

1. The first step consists of the formation of different stable solutions of the alkoxide or metal precursors solvent.
2. Fuel precursor has to be chosen carefully
3. In the second step, gelation begins, which results in the formation of an oxide or alcohol-bridged network (the gel).
4. Heat is needed to start combustion process automatically after the gel is made. Temperature may vary for different samples and different conditions. Samples were heated continuously.
5. After a certain temperature auto-combustion process starts and the gel begins to burn. NPs can be found from the ashes of the gel.
6. pH must be maintained at 7.0

That's how NPs can be found by auto-combustion technique [61-63].

2.11. Photo-catalytic Activity

Photo-catalysis is the amalgamation of photochemistry and catalysis. The word “photo-catalysis” is derived from the Greek language and composed of two parts:

- The prefix photo means light
- Catalysis is the process where a substance involves in altering the rate of a chemical transformation of the reactants without being altered in the end. The substance which is known to be a catalyst increases the rate of the reaction by reducing the activation energy.

Hence, photo-catalysis is a process where light and catalysts are concurrently used to support or speed up a chemical reaction. So, photo-catalysis can be defined as “catalysis driven acceleration of a light-induced reaction.”

The photo-catalyst is an extraordinary method which can be used for various purposes like degradation of various organic pollutants in wastewater, production of hydrogen, purification of air and antibacterial activity. Recently, the photo-catalytic process is attaining more concentration in the field of wastewater treatment to two basic Principles, Mechanism, and Challenges of Photo-catalysis obtain complete mineralization of the pollutant achieved under mild conditions of temperature and pressure. The noteworthy features of these processes include undisposed of waste and cost-effectiveness when sunlight or near-UV light or Visible light can be used as a source of irradiation. Photo-catalyst is a term which means photon assisted generation of catalytically active species. In general, Photo-catalysis can be defined as “a change in the rate of chemical reactions or their generation under the action of light in the presence of substances called photo-catalyst that absorbs light quanta and is involved in the chemical transformations of the reactants”

2.11.1 Photo-catalytic mechanism

Photo-catalytic reaction primarily depends on wavelength or light (photon) energy and the catalyst. In general, semiconducting materials are used as a catalyst which performs as sensitizers for the irradiation of light stimulated redox process due to their electronic structure, which is characterized by a filled valence band and a vacant conduction band. Fig.4 shows the schematic representation of semiconductor photo-catalytic mechanism. The fundamental steps in the process of semiconductor photo-catalysis are as follows.

- When the light energy in terms of photons fall on the surface of a semiconductor and if the energy of incident ray is equivalent or more than the band gap energy of the semiconductor, the valence band electrons are agitated and move to the conduction band of the semiconductor.
- Holes would be left in the valence band of the semiconductor. These holes in the valence band can oxidize donor molecules and react with water molecules to generate hydroxyl radicals (The hydroxyl radicals have strong oxidizing power responsible for the degradation of pollutants).

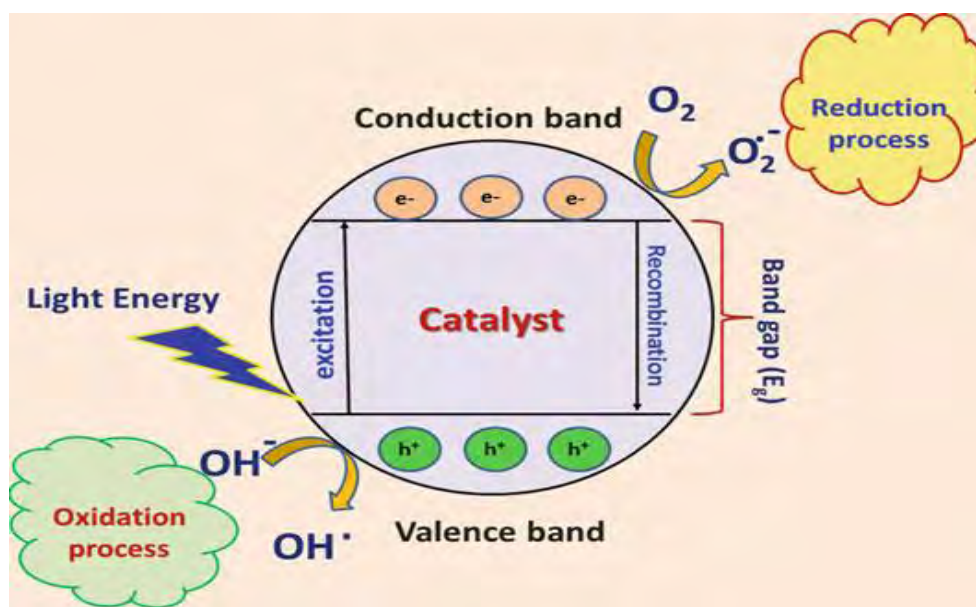


Fig. 4: Schematic representation of semiconductor photo-catalytic mechanism

- The conduction band electrons react with dissolved oxygen species to form superoxide ions. These electrons induce the redox reactions.
- These holes and electrons could undergo successive oxidation and reduction reactions with any species, which might be adsorbed on the surface of the semiconductor to give the necessary products.

2.11.2 Description of oxidation mechanism

The photo-catalyst surface contains water, which is mentioned as “absorbed water”. This water is oxidized by positive holes created in the valence band due to the electrons shift to the conduction band as a result of light irradiation, thus making way for the formation of hydroxyl ($\text{OH}\cdot$) radicals (agents which have strong oxidative decomposing power).

Afterward, these hydroxyl radicals react with organic matter present in the dyes. If oxygen is present when this process happens, the intermediate radicals in the organic compounds along with the oxygen molecules can experience radical chain reactions and consume oxygen in some cases. In such a case, the organic matter finally decomposes ultimately becoming carbon dioxide and water [65, 66]. Under such circumstances, organic compounds can react straightly with the positive holes, resulting in oxidative decomposition. The complete oxidation processes were shown in Fig. 5.

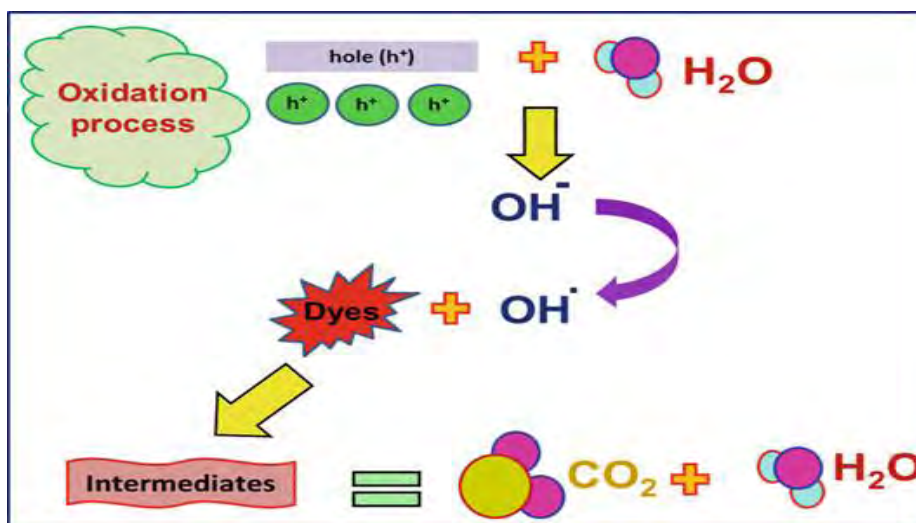


Fig. 5: Schematic representation of oxidation mechanism

2.11.3 Description of reduction mechanism

Fig. 6 represents the reduction process, the reduction of oxygen contained in the air occurs as a pairing reaction [67]. Reduction of oxygen takes place as an alternative to hydrogen generation due to the fact that oxygen is an easily reducible substance. The conduction band electrons react with dissolved oxygen species to form superoxide anions. These superoxide anions attach to the intermediate products in the oxidative reaction, forming peroxide or changing to hydrogen peroxide and then to water. The reduction is likely to occur more easily in organic matter than in water. Therefore, the higher concentration of organic matter tends to increase the number of positive holes. This reduces the carrier recombination and enhances the photo-catalytic activity [67].

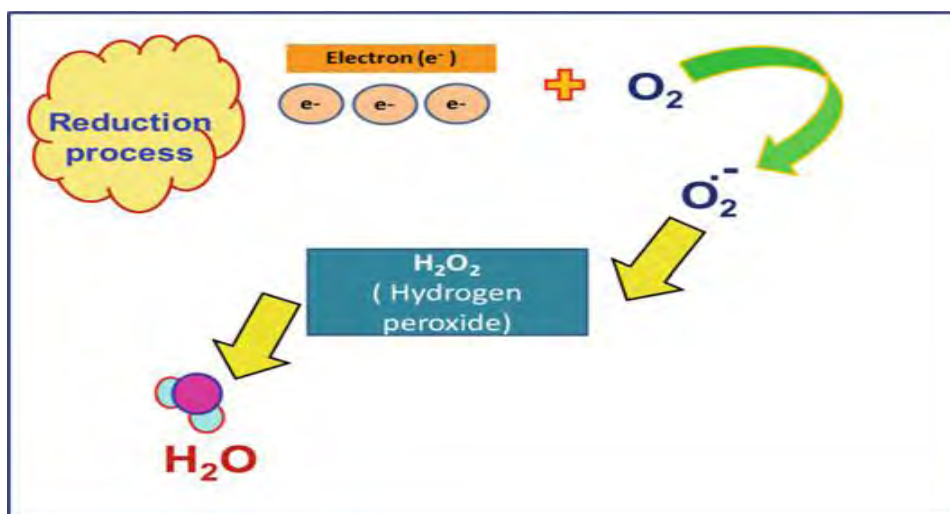


Fig. 6: Schematic representation of reduction mechanism

2.11.4 Operating and affecting parameters of photo-catalysis

The rate of photo mineralization of an organic compound by photo-catalysis method primarily depends on the following parameters: structure, shape, size, and surface area of the catalyst, reaction temperature, pH, light intensity, amount of catalyst, and concentration of wastewater [68].

2.11.4.1 Crystal structure, shape, size, and surface area of catalyst

The structure of catalyst plays a key role in achieving superior photo-catalytic activity. For example, TiO₂ material has three phases such as anatase, rutile and brookite. But the most sensitive and attractive phase is the anatase phase having a notable photo-catalytic activity due to its stability, the position of the conduction band, the higher degree of hydroxylation and adsorption power [69]. On the other hand, morphology also acts as a potential factor that influences the final degradation efficiency which was reported earlier [68]. It is reported that spherical-shaped CuO samples show higher efficiency compared with the spindle and rod-shaped CuO samples due to its large surface area. Nanomaterials having large surface area and smaller size are compared with bulk materials so that it can effectively show higher efficiency in the photo-catalytic reaction. When compared with bulk CuO, the nanosized CuO material shows more efficient for water purification and recycling ability due to their smaller size [70]. When the size of the catalyst is smaller, a huge number of atoms are accumulated on the surface of a catalyst which leads to increase in surface to volume ratio. This property enhances number of active sites and interfacial charge carrier transfer rates thereby achieving higher catalytic activities. And also it is well known that the photo-catalytic redox reaction mainly takes place on the surface of the photo-catalysts and so the surface properties significantly influence the efficiency of catalyst [71].

2.12 Characterization Techniques:

2.12.1 X-Ray Diffraction (XRD)

The phenomenon of XRD is based upon the interaction of X-rays with the periodic atomic structure of crystals. German scientist Max von Laue in 1912 first made the point that, “if crystals were composed of regularly spaced atoms which act as scattering centers for X-rays, and if X-rays were electromagnetic wave of wavelength about equal

to the interatomic distance in crystals, then it should be possible to diffract X-rays by means of crystals” [71]. Under his direction the first attempt of experiments to test this hypothesis was made by Friedrich and Knipping, and they were successful (at their second attempt) in proving the wave nature of X-ray and the periodicity of atom arrangement in crystals. However, it was the English physicist W. H. Bragg and his son W. L. Bragg, who successfully analyzed the Laue experiment, and expressed the necessary conditions for diffraction in a simple mathematical form.

2.12.1.1 Principle

In case of XRD, X-rays impinge upon the different atoms in the crystal, and are scattered. When these scattered rays interfere with each other they cause a variation in amplitude for different scattered directions, those directions with large amplitude being considered as diffracted rays. In the scattering process, if there is a difference in the length of path travelled by the incident and scattered rays this leads to difference in phase and to different interference conditions and thus different strength diffraction in various directions. We can view the interaction of X-rays with a crystal as due to reflection from atomic planes, see Fig-7. In Fig-7, the necessary conditions for diffraction in a crystal are described.



Fig.7: A Philips PW 3040 X'Pert Pro X-ray diffractometer

2.12.1.2 Bragg's Law

When an incident X-ray beam makes an angle ϕ with respect to the lattice planes (this angle ϕ is equal to the angle of reflection), a diffracted beam may be formed.

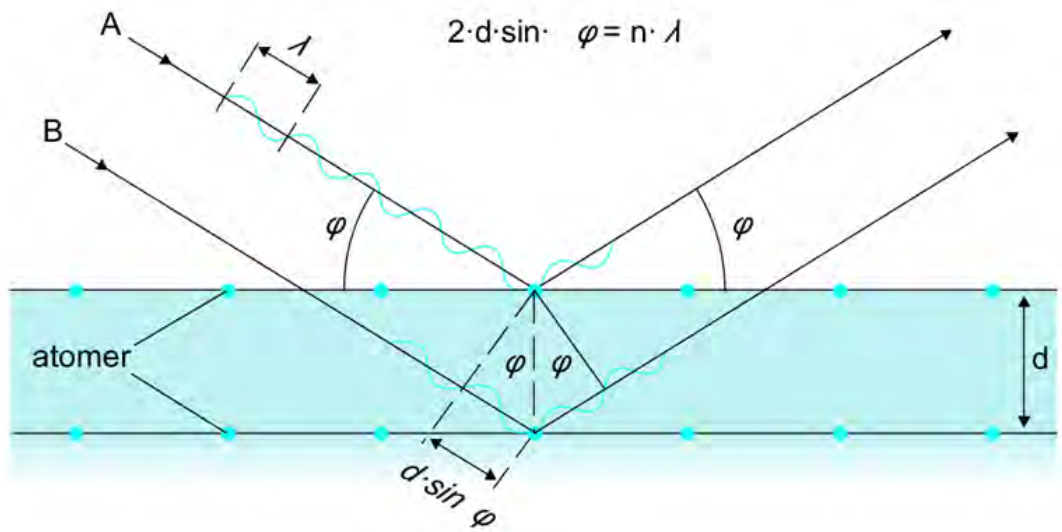


Fig. 8: Bragg's diffraction pattern

Fig. 8: shows diffraction of X-rays by a crystal, where d is the difference between crystal planes. Reflected rays A and B will be completely in phase if this path difference is equal to whole number n of wavelength, or if

$$n\lambda = 2d\sin\phi$$

This relation was proposed by W.L. Bragg and is known as Bragg's law. It states the essential conditions which must be met if diffraction from a set of planes is to occur. n is called the order of diffraction. It may be any integral value which is consistent with $\sin\phi$ not exceeding unity and is equal to the number of wavelengths in the path difference between rays scattered by adjacent planes. Therefore for fixed values of λ and d , there may be several angles of incidence $\phi_1, \phi_2, \phi_3, \dots$ at which diffraction may occur, corresponding to $n=1, 2, 3, \dots$. So in a first order diffraction ($n=1$), the scattered rays A and B of Fig-4 would differ in path length (in phase) by one wavelength. The rays scattered by all the atoms in all planes are therefore completely in phase, and reinforce one another (constructive interference) to form diffracted beam in the direction shown. In most other directions of space the scattered beams are out of phase, and null each other (destructive interference). The diffracted beam is generally weak compared to the incident beam as the plane reflects only a small fraction of the energy incident on them. So in summary, we can say in a perfect crystal atoms are arranged periodically in space, in a few directions, those satisfying Bragg's law. The scattering is strong, as a result diffraction is observed. The angle at which diffracted beams are seen

allow one to deduce the interplanar spacing d . Thus one can identify the composition of samples, their state of strain, material texture and crystallite size.

2.12.1.3 XRD setup:

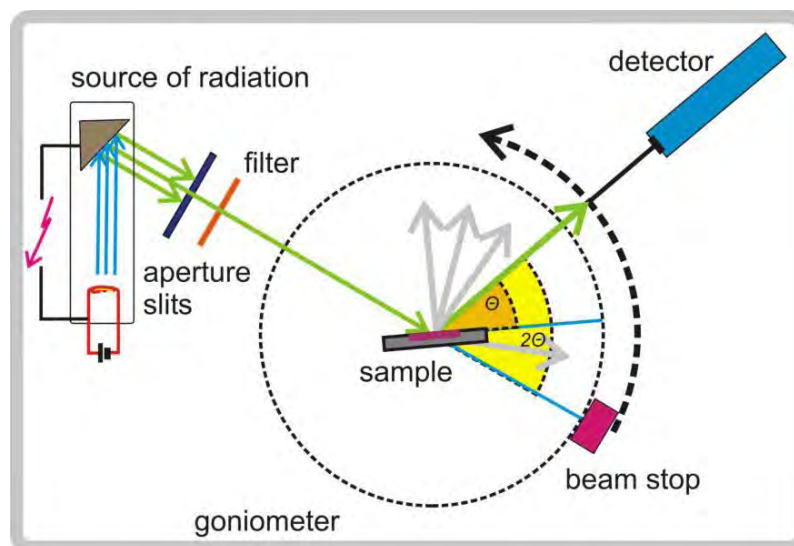


Fig. 9: A simple diagram of optics used in the XRD instrument.

In XRD, a collimated beam of X-rays typically ranging from 0.5-2.5 Å is used as a source [16]. For diffraction a monochromatic X-ray source is needed and the source is generally a metal anode bombarded by high energy electrons which gives off both characteristics line spectrum X-rays and continuum (Bremsstrahlung) radiation. Generally, the stronger $k\alpha$ radiation is used and $k\beta$ radiation is filtered. In our system, Cu $k\alpha$ radiation is used where $\lambda=1.54 \times 10^{-10}$ m. The purpose of the Gobble mirror (a curved mirror) is to collimate the divergent beam coming from the point-like source in the X-ray tube anode. The mount in the diffractometer where the sample sits is called the goniometer. The goniometer allows the altering of orientation of the sample. Depending on the number of degrees of freedom of goniometer, and the allowed movement of the source and/or the detector the XRD system can be called a ‘one-circle’, ‘two-circle’ diffractometer etc. The diffractometer used for this thesis work is a ‘four-circle’ diffractometer, a three circles goniometer plus a movable detector. The function of the solar slit is to remove any randomly scattered nonparallel X-rays. The detector used is a scintillation detector, which is a single photon detector. When the incident X-ray strikes the fluorescent crystal (scintillator) at the front of the detector a

visible photon is produced. A photocathode struck by a photon ejects an electron. A series of dynodes after the scintillator/photocathode amplifies the electron into a detectable electrical pulse.

As stated earlier in the discussion of Bragg's law using XRD one can address issues related to crystal structure of solids. The crystal information which can be extracted includes-

1. Identification of unknown materials phases
2. Lattice constant and symmetry measurement
3. Orientation of single crystals and preferred orientation of poly-crystals
4. Crystal quality (of bulk and thin crystal phases) measurement
5. Quantification of crystal defects, stress etc.

In addition, it is a non-destructive technique. Different XRD modes are used to examine the nanostructures grown in this work as follows-

- **θ - 2θ mode:** This mode is used to study which crystallite planes are parallel to the substrate surface, and thus give evidence either for deposit poly-crystallinity or texture. The angle between the source and the scattered beam (2θ) at which diffraction is seen defines the interplanar spacing (d) of the layers responsible. The symmetrical source/scatter beam arrangement means we only see contribution from planes parallel to the substrate.
- **ω (or rocking curve) mode:** In case any evidence is found for texture structure in the θ - 2θ mode, this mode reveals the degree of preferential alignment.
- **ϕ mode:** This mode is to study the in-plane alignment to determine epitaxial relationship if there is evidence of highly textured growth. [72].

2.12.2 Field Emission Scanning Electron Microscope (FESEM)

FESEM is a technique that uses electrons as a substitute of light to form an image. Since their development in the early 1950's, FESEM has allowed researchers to examine a much bigger variety of specimens. FESEM has a large depth of field, which allows more of a specimen to be in focus at one time, FESEM also has much higher resolution, so closely spaced specimens can be magnified at much higher levels. Because FESEM uses electromagnets rather than lenses, the researcher has much more control in the degree of magnification [73, 74]. It is an instrument that produces a largely magnified

image by using electrons instead of light to form an image. A beam of electrons is produced at the top of the microscope by an electron gun and the electron beam follows a vertical path through the microscope, which is held within a vacuum, the beam travels through electromagnetic fields and lenses, which focus the beam down towards the sample. Once the beam hits the sample, electrons and X-rays are ejected from the sample, as can be observed in Fig-10. The detectors collect these X- rays, backscattered electrons, and secondary electrons and convert them into a signal that is sent to a screen similar to a television screen, which produces the final image. It is generally of non-destructive nature, though sometimes it can cause sample damage due to high energy electron beam irradiation. [74]

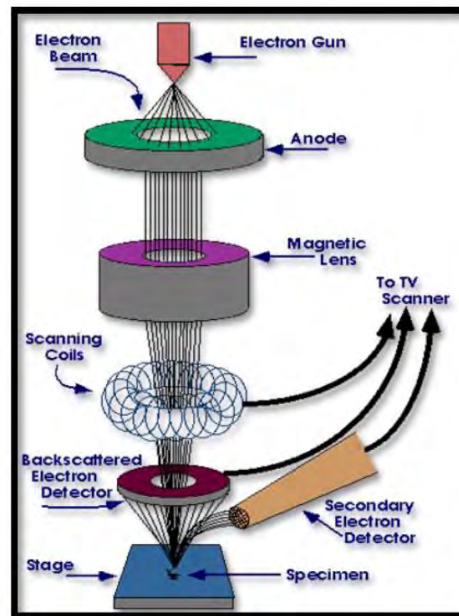


Fig. 10: Schematic diagram of FESEM

2.12.2.1 Principle

When an electron beam bombards a solid surface, the incident electrons are scattered. The electron scattering can be divided into two categories, elastic and inelastic scattering, but the speed remains constant. Hence, the kinetic energy of the incident electron remains the same. During an inelastic event, part of the energy of the incident electron is transferred to its colliding partner. Secondary electron, Auger electrons and X-ray are produced by the inelastic scattering events, as shown in the following fig. 10

A **Field Emission SEM (FESEM)** is a type of SEM where a field-emission cathode in the electron gun of a SEM provides narrower probing beams at low currents as well as high electron energy, resulting in both improved spatial resolution and minimized sample charging, and damage. It is used for applications which demand the highest magnification possible. The types of signals produced by a SEM as shown in Fig.10 include, secondary electrons (SEs), back-scattered electrons (BSE), characteristic X-rays, light, specimen current (LSC), transmitted electrons (TE) and Auger electrons (AE). SEs are sample electrons excited from the top surface layer of the specimen (0-10 nm). They are defined as having energy range 0-50 eV with the majority having energy of 3 to 5 eV. They produce the image of the surface of the sample and give information on sample topography. The emission of secondary electrons from each point on the specimen surface is dependent on its shape. BSEs are scattered beam electrons that emerge from greater depths in the sample. They are defined as electrons those having energy greater than 50 eV with the majority having energy approximately $\frac{3}{4}$ of the incident electron beam (probe energy). The number of BSEs that are emitted is strongly dependent on the mean atomic number of the specimen at the point of impact of the beam. So, as the atomic number increases, the greater the number of electrons that are backscattered. BSEs give depth information and atomic number contrast within the image. Thus, BSE images can provide information about the distribution of different elements in the sample. Characteristic X-rays are emitted when the electron beam removes an inner shell electron from the sample, causing a higher energy electron to fill the shell and release energy as an X-ray with characteristic energy. These characteristic X-rays are used to identify the atomic composition, and measure the abundance of elements in the sample. CL light is generated by some specimens that contain electroluminescent materials. CL will be described in more detail in the next section of this chapter. SC is the electron flow out of the specimen to earth, and if an amplifier is placed in the return path of electrons to earth its value can be measured, and can be also be used for imaging. TEs can be detected provided the sample is exceptionally thin. AE are un-scattered electrons produced via ionization of sample atoms, and have energies characteristic of the atoms.



Fig. 11: A Photo of FESEM JSM-7600F

The most common or standard detection mode, secondary electron imaging or SEI is used to produce two-dimensional scan with topographical feature information about the specimen. Secondary electron detectors are common in all SEMs, but it is rare that a single machine would have detectors for all possible signals. The signals result from interactions of the electron beam with atoms at or near the surface of the sample. SEM can produce very high-resolution image at or near the sample surface revealing details at nm scales due to the small wavelengths of higher energy electrons which allows better microscopic resolution. In case of field emission this resolution is much better and produces clearer, less electrostatically distorted images. Also, high quality, low voltage images are obtained with negligible electrical charging of samples [19].

The FESEM instrument used for much of the present thesis work is a JEOL JSM 7500F field emission system as shown in Fig-11. The JEOL JSM 7500F is a computer controlled high resolution FESEM which produces exceptional images at both normal and low operating voltages.

2.12.3 Fourier Transform Infrared Spectrometer (FTIR)

FTIR stands for Fourier Transform Infrared, where some of the infrared radiation is absorbed by the sample and some of it passes through (transmitted). The resulting

spectrum represents the molecular absorption and transmission, creating a molecular fingerprint of the sample [20]. It can identify unknown materials, can determine the quality or consistency of a sample and can determine the number of components in a mixture [20, 21].

These instruments separate the individual frequencies of energy emitted from the infrared source. An infrared prism works exactly the same as a visible prism which separates visible light into its colors (frequencies). The detector measures the amount of energy at each frequency which has passed through the sample [22]. Fourier transform infrared spectroscopy is preferred over dispersive or filter methods of infrared spectral analysis for the following reasons:

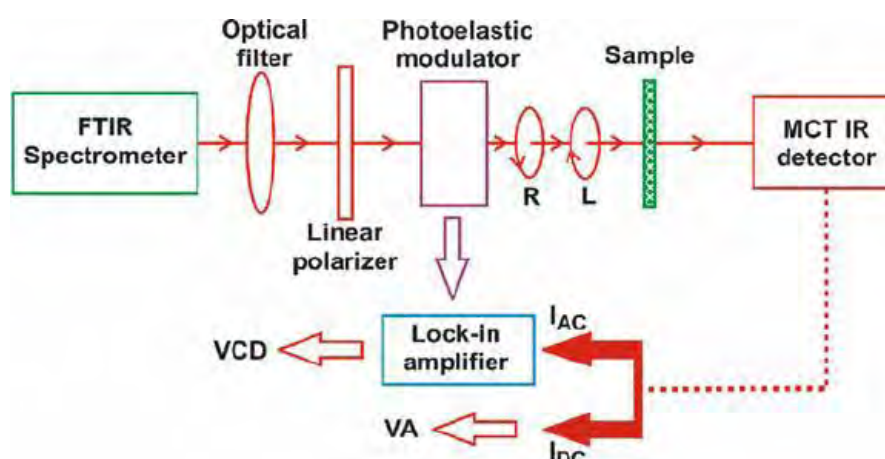


Fig. 12: Schematic illustration of an FTIR system

- It is a non-destructive technique.
- It can increase speed, collecting a scan every second.
- It can increase sensitivity within one second scans can be co-added together to ratio out random noise.
- It has greater optical throughput.
- It is mechanically simple with only one moving part.

Fourier Transform Infrared (FTIR) spectrometry was developed in order to overcome the limitations encountered with dispersive instruments. The main difficulty was the slow scanning process. Method for measuring all of the infrared frequencies

simultaneously, rather than individually, was needed. A solution was developed which employed a very simple optical device called an interferometer [77]. Thus, the time element per sample is reduced to a matter of a few seconds rather than several minutes. Most interferometers employ a beam splitter which takes the incoming infrared beam and divides it into two optical beams. One beam reflects off of a flat mirror which is fixed in place. The other beam reflects off of a flat mirror which is on a mechanism which allows this mirror to move a very short distance (typically a few millimeters) away from the beam splitter [76]. The two beams reflect off of their respective mirrors and are recombined when they meet back at the beam splitter, this is because the path that one beam travels is a fixed length and the other is constantly changing as its mirror moves, the signal which exits the interferometer is the result of these two beams “interfering” with each other. The resulting signal is called an interferogram which has the unique property that every data point (a function of the moving mirror position) which makes up the signal has information about every infrared frequency which comes from the source. This transformation is performed by the computer which then presents the user with the desired spectral information for analysis.

2.12.3.1 FTIR peak analysis

There are about 20 main asymmetric absorption bands which are typical for high molecular compounds with irregular structure. Spectra differ from each other in band's intensity, but the number of bands and their frequencies are similar. Strong wide band between 3500 cm^{-1} – 3100 cm^{-1} assigned to O-H stretching vibrations. This band is caused by presence of alcoholic and phenolic hydroxyl groups involved in hydrogen bonds. The intensity of the band increases during demethylation and decreases during methylation since during demethylation the O-CH₃ bonds in methoxyl groups bonded to 3rd or 5th carbon atom of the aromatic ring is splinted and CH₃ is replaced by a hydrogen atom producing a new OH group. During methylation the O-H bonds are splinted and H is replaced by CH₃ group and amount of OH group is decreasing hence intensity of the band is decreasing [75].

Bands at 2920 cm^{-1} and 2850 cm^{-1} to C–H stretching vibrations of the methoxyl group. Absorption bands caused by stretching vibrations of carbonyl groups are located in the $(1765\text{-}1615)\text{ cm}^{-1}$ wavenumber range.

The absorption band at 1660 cm^{-1} is referred to conjugated carbonyl groups. The absorption band at 1720 cm^{-1} is assigned to carboxyl group. Stretching vibrations of C=C bonds are found in the $(1608-1626)\text{ cm}^{-1}$ region. Deformation vibrations of C-H bonds related to double bonds are normally located in the region $(988-960)\text{ cm}^{-1}$.

IR spectra of absorption band at $(1585-1580)\text{ cm}^{-1}$, assigned to aromatic rings, conjugated with α -carbonyl group. As regarding absorption bands at 1465 cm^{-1} and 1420 cm^{-1} , there is no consensus concerning their assignment. The absorption band at 1420 cm^{-1} to deformation vibrations of the C-H group in the aromatic ring. On the other hand, the absorption band at 1420 cm^{-1} relates to symmetric bending vibrations of C-H bonds in methoxyl groups, while the band at 1465 cm^{-1} was assigned to both CH_2 -, and OCH_3 - groups [23].

The band at $(1450-1420)\text{ cm}^{-1}$ to aromatic ring vibrations. The absorption band at 1430 cm^{-1} both to asymmetric deformation vibrations of C-H bonds in methoxyl groups and to vibrations of the aromatic ring. The absorption bands at 1360 cm^{-1} and 1210 cm^{-1} are caused by vibrations of phenolic hydroxyls.

The absorption bands at 1380 cm^{-1} and 1340 cm^{-1} to phenolic hydroxyls and absorption bands at 1365 cm^{-1} to symmetric deformation vibrations of C-H in methoxyl groups. Pilipchuk observed an intensity increase of the absorption bands at 1370 cm^{-1} in the spectra of methylated and acetylated lignin samples while the bands are absent in the demethylated lignin spectra. Hence the absorption bands were assigned to symmetric deformation vibrations of C-H in methoxyl groups [76].

The intensity increases of the absorption band between $(1240-1210)\text{ cm}^{-1}$ in the spectra of methylated and acetylated lignin allows to relate the band to asymmetric stretching vibrations of the C-O-C linkages in ethers and esters or to phenolic hydroxyls [75].

The bands at 1190 cm^{-1} , 1125 cm^{-1} and 1031 cm^{-1} originates from methoxyl groups and the bands at $(1090-1075)\text{ cm}^{-1}$ and 1040 cm^{-1} emanates from primary and secondary alcoholic groups. The absorption bands at 1160 cm^{-1} and 1040 cm^{-1} to deformation vibrations of the C-H bonds on benzene rings.

The bands at 1100 cm^{-1} , 1072 cm^{-1} and 1033 cm^{-1} might be caused by vibrations of C=O bonds in primary and secondary alcoholic groups and the bands at 1130 cm^{-1} and 1030 cm^{-1} might be caused by dialkyl ether bonds [75].

2.12.4 UV-Visible Spectroscopy

An instrument used in the ultraviolet-visible spectroscopy is called UV-Visible spectrometer. The wavelength of UV is shorter than the visible light. It ranges from 100 to 400 nm. In a standard UV-Vis spectrophotometer, a beam of light is split; one half of the beam (the sample beam) is directed through a transparent cell containing a solution of the compound being analyzed, and one half (the reference beam) is directed through an identical cell that does not contain the compound but contains the solvent. The instrument is designed so that it can make a comparison of the intensities of the two beams as it scans over the desired region of the wavelengths. If the compound absorbs light at a particular wavelength, the intensity of the sample beam (I_S) will be less than that of the reference beam. Absorption of radiation by a sample is measured at various wavelengths and plotted by a recorder to give the spectrum which is a plot of the wavelength of the entire region versus the absorption (A) of light at each wavelength. And the band gap of the sample can be obtained by plotting the graph between ($\alpha h\nu$ vs $h\nu$) and extrapolating it along x-axis. Ultraviolet and visible spectrometry is almost entirely used for quantitative analysis; that is the estimation of the amount of a compound known to be present in the sample. The sample is usually examined in solution [23].



Fig. 13: Schematic diagram of UV-Visible spectrometer

CHAPTER 3

EXPERIMENTAL METHODS AND CHARACTERIZATION TECHNIQUES

A detailed description about nanoparticle creation technique used in my thesis (sol-gel auto-combustion method) is discussed briefly in this chapter. Besides different characterization techniques used for analyzing prepared NPs are discussed here.

3.1 Precursors

Copper nitrate ($\text{Cu}(\text{NO}_3)_2 \cdot 3\text{H}_2\text{O}$), Cerium Nitrate Hexahydrate [$\text{Ce}(\text{NO}_3)_4 \cdot 6\text{H}_2\text{O}$] were used as precursors for Cu and Ce (99% pure). Citric acid acts as fuel here. Fuel & Oxygen ratio plays a vital ratio here. Copper oxide has two stable oxide form as CuO and Cu_2O . Formation of either CuO or Cu_2O depends on this fuel & oxygen ratio. A favorable fuel oxygen ratio has been chosen. Water was used as solvent in the preparation process. NH_3 solution was used for changing the acidic solution to normal solution by increasing pH to 7.0. An overview of required chemicals is shown below.

3.2 Synthesis of CuO and Ce Doped CuO NPs

3.2.1 Experimental setup

CuO NPs were prepared via a simple sol-gel auto-combustion route at low temperature and low-cost method. A magnetic stirrer with heater required for preparing CuO NPs. Some beakers and a glass rod with this magnetic stirrer are enough for synthesizing NPs.



Fig 14: Experimental setup for the preparation of CuO & Ce doped CuO NPs.

3.2.2 Synthesis of pure CuO NPs

CuO NPs were prepared using copper nitrate tri-hydrate as a copper precursor and citric acid as a fuel. These precursor and fuel were taken to two separate 500 ml beaker at room temperature. Sufficient distilled water was added to these beakers to make solution. Magnetic stirrer was used for dissolving copper nitrate and citric acid into water and creates white solution after dissolving into water. The solutions were mixed for approximately twenty minutes under constant stirring. After that the citric acid solution was added to copper nitrate solution. That is the final solution for preparing CuO NPs [78-80].

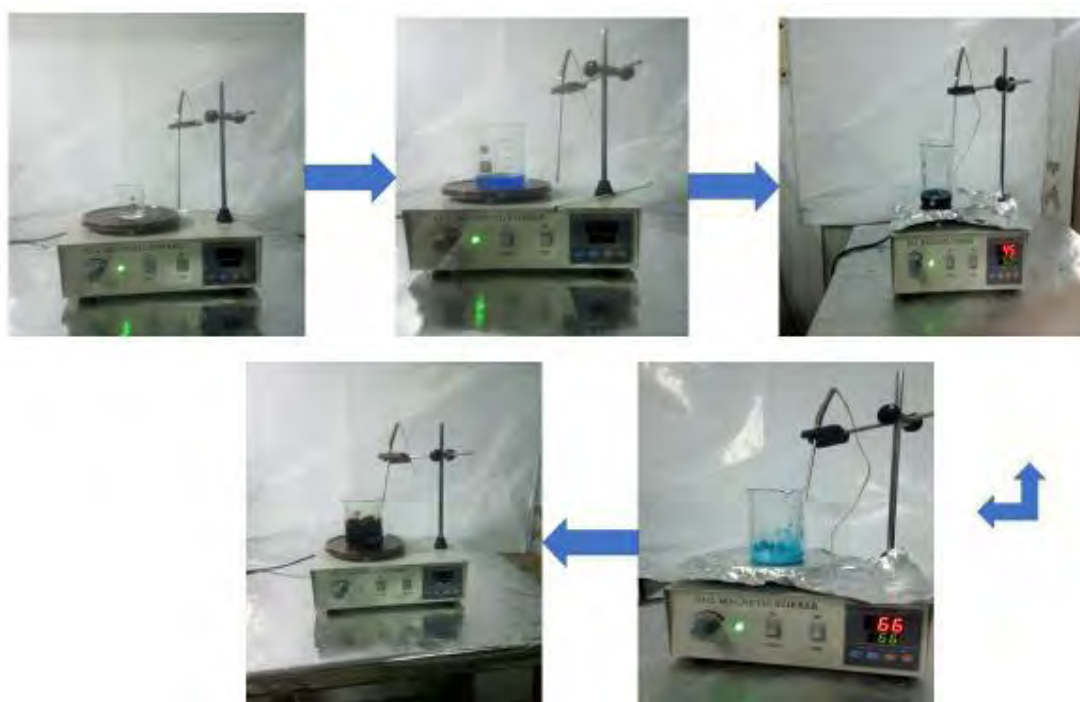


Fig 15: Synthesis process of CuO NPs

3.2.2.1 Conditions

1. As earlier mentioned, fuel and oxygen ration plays a vital role here. The more citric acid in the solution, the easier the auto-combustion. For easy auto-combustion process fuel : oxidant ratio was selected as 1:1. To do so, some calculations were performed; Atomic mass of copper nitrate and citric acid is 241.6 gm and 192 gm respectively. As to maintain fuel oxidant ratio, it should be 241.6 :192. But this huge amount NPs were not necessary to be created. So copper nitrate and citric acid were taken as 24.16 gm and 19.2 gm.

Chapter 3: Experimental methods and characterization techniques

2. pH plays a major role in this experiment. For getting good NPs it is required to put a constant pH value at 7.0.

The color of $\text{Cu}(\text{NO}_3)_2 \cdot 3\text{H}_2\text{O}$ and citric acid was blue and white respectively. Both solutions were prepared separately. When citric acid solution was added to copper nitrate solution it turns into green solution. Besides color changes, pH changes drastically to 1.0. But pH 7.0 is required to acquire good quality nanoparticle. This solution was placed on hotplate with magnetic stirrer. This solution needs to be stirred constantly. At this stage, the heater was started. Initially the temperature was low, almost 50 degree. At this temperature the solution gets mixed properly as well as pH needs to be adjusted. A pH meter or analogous pH paper is required to check solutions pH. To increase pH value, NH_3 solutions were added. The pH value needs to check simultaneously while adding NH_3 solution for safety. Otherwise if solutions pH become more than 7.0, acidic solution needs to be added. After the solutions pH becomes 7.0, then the temperature was raised gradually. But it is better to maintain (50-60) degree temperature while gel formation. After gel is formed, then let citric acid be performed as fuel and start auto-combustion. While increasing heater temperature to 80-90 degree, the gel began to burn. The CuO NPs were found from the ashes of the burned gel.

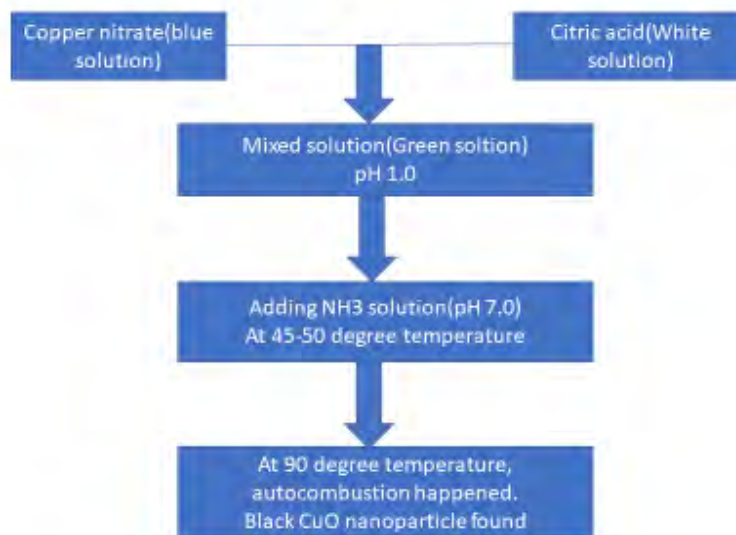


Fig 16: Schematic diagram of preparation of CuO NPs.

3.3 Synthesis of Ce doped CuO NPs

Our research also represents the Ce doping effect on CuO NPs. Ce NPs were doped at 2%, 4%, 6% and 8 mole% concentration. The procedure of Ce NPs on CuO are given below:

3.3.1 Required Chemicals: The amount of required chemicals is given in table 2.

Table 2: Required chemicals for preparing pure and Ce doped CuO NPs.

Samples	Cu(NO ₃) ₂ ·3H ₂ O (mole%)	[Ce(NO ₃) ₃ ·6H ₂ O] (mole%)	Citric acid(C ₆ H ₈ O ₇)(mole%)
Pure CuO	100%	0%	100%
2% Ce doped CuO	98%	2%	100%
4% Ce doped CuO	96%	4%	100%
6% Ce doped CuO	94%	6%	100%
8% Ce doped CuO	92%	8%	100%

3.3.2 Preparation of Ce doped CuO NPs

The preparation procedure of Ce doped CuO NPs remain almost same as pure CuO NPs. The additional step for doped CuO is just addition of Ce(NO₃)₃·6H₂O aqueous solution. An aqueous solution of Ce(NO₃)₄·6H₂O was prepared. The necessary amount of Ce(NO₃)₃·6H₂O is showed in Table 2. The solution of Cu(NO₃)₂·3H₂O and Ce(NO₃)₃·6H₂O was added in a beaker. Then the solution turns into green color. pH of the solution tends to almost 1.0 for all doped CuO NPs samples. After that citric acid was added slowly in that solution. To increase pH of these solutions to 7.0, NH₃ solution was added. Addition of NH₃ solution to the beaker makes the color black. The rest procedure is same as preparation of pure CuO NPs.

3.4 XRD Experimental Setup



Fig. 17: Instrumental setup for XRD measurement.

3.5 Field Emission Scanning Electron Spectroscopy setup



Fig. 18: FESEM setup for taking images of NPs

3.6 UV-Visible Experimental Setup:



Fig. 19: UV-Vis experimental setup

3.7 FTIR Setup:



Fig. 20: FTIR setup for experimental setup.

3.7 Photo-catalysis Activity Experimental Setup:



Fig. 21: Homemade photo-catalytic chamber

CHAPTER 4

RESULTS AND DISCUSSION

In the previous chapter, we discussed the synthesis procedure of CuO and Ce doped CuO NPs. In this chapter we will discuss the analysis process and the obtained result from the characterization analysis.

4.1 Sample Preparation Procedure for Characterization:

- ❖ For FESEM analysis, all prepared samples were dissolved in Isopropanol. Then the samples were ultrasonic sized by ultrasonic probe. Samples were in a 50ml vial. Then using ultrasonic probe, the particles were properly separated in the solution. After this, 2-3 droplets samples were taken from the solution and dried it to room temperature. This process helps to take clearer FESEM images.
- ❖ For XRD characterization, samples were annealed at 500C temperature. A furnace was used for annealing NPs. All of the samples were annealed at the same temperature. After annealing, the samples were ready for XRD characterization.
- ❖ Sample procedure for FTIR and XRD remains same.
- ❖ For optical analysis, our prepared samples were used in UV-Visible optical analysis. No need to further processing.
- ❖ For Raman Spectroscopy analysis no further processing is required.

Now our sample is prepared. It is time to characterize the samples. The results were obtained from different characterization is discussed below:

4.2 Field Emission Scanning Electron Microscopy (FESEM)

The morphology of pure and Ce doped CuO NPs were studied by FESEM. fig. 22 shows the magnified FESEM micrographs for pure CuO, 2%, 4%, 6% and 8 mole% Ce doped CuO samples respectively. These figures show the presence of fine spherical aggregates of smaller individual NPs of various sizes. It is clear from the highly magnified images of our samples shown in the figure. The pure and Ce doped CuO particles exhibit uniform shape and narrow size distribution with particle size in the range of (14–20) nm. After the incorporation of Ce with CuO the particle size reduced to 20 nm to 14 nm with increasing the Ce concentration up to 8 mole% and the distribution of size become more uniform. The trend of the reduction of grain size of NPs matches with the observations of XRD spectra. All these images confirm that Ce is successfully doped in CuO nanostructure

and the particles are composed of many single crystallites of varying size and orientation without any major lattice defects.

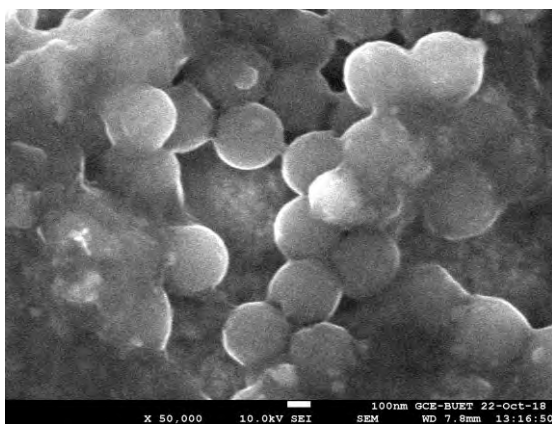


Image: a

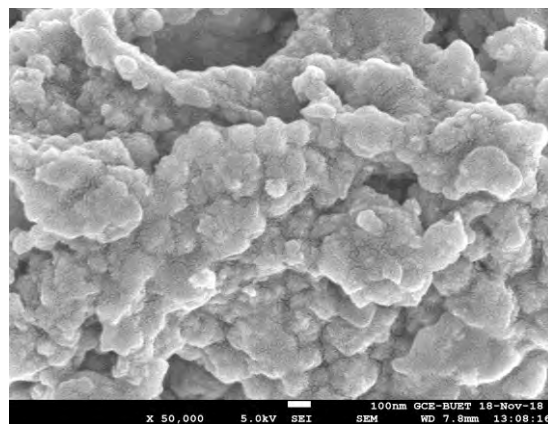


Image:b

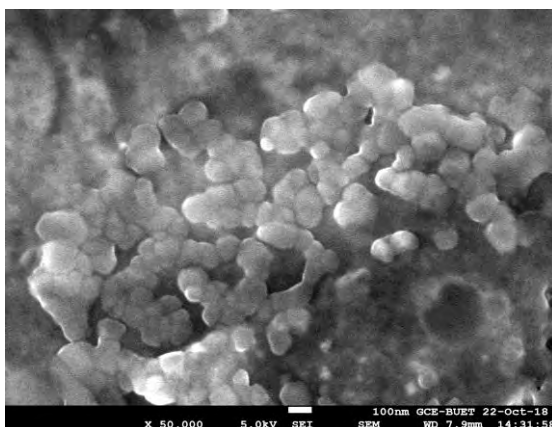


Image: c

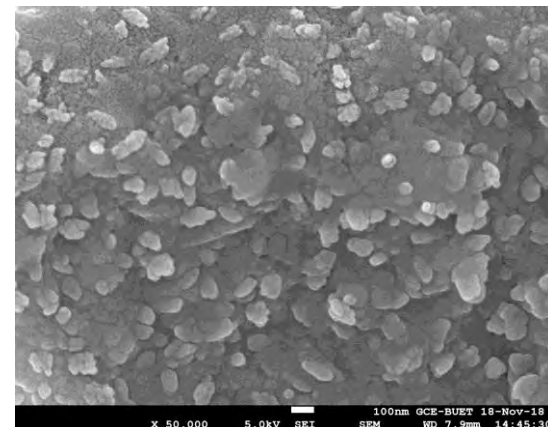


Image: d

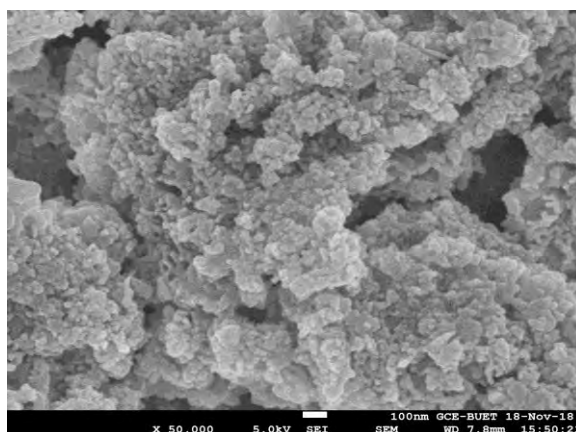


Image: e

Fig.22: FESEM images of (a) Pure CuO, (b) 2 mole% Ce, (c) 4 mole% Ce, (d) 6 mole% Ce, (e) 8 mole% Ce doped CuO NPs.

4.3 EDS Analysis

Fig.23 shows the elemental analyses of pure CuO NPs and Ce doped CuO NPs analyzed by EDS. It is obviously observed that the EDS spectrum of pure CuO NPs only contains Cu element and O element, which demonstrates that the resultant NPs are pure CuO NPs. The EDS result of Ce doped CuO NPs presents that except for Cu and O elements, Ce element is also contained in the NPs. No other peak associated with impurities is observed in Fig. 23 indicating that the fabricated NPs are Ce-doped CuO NPs.

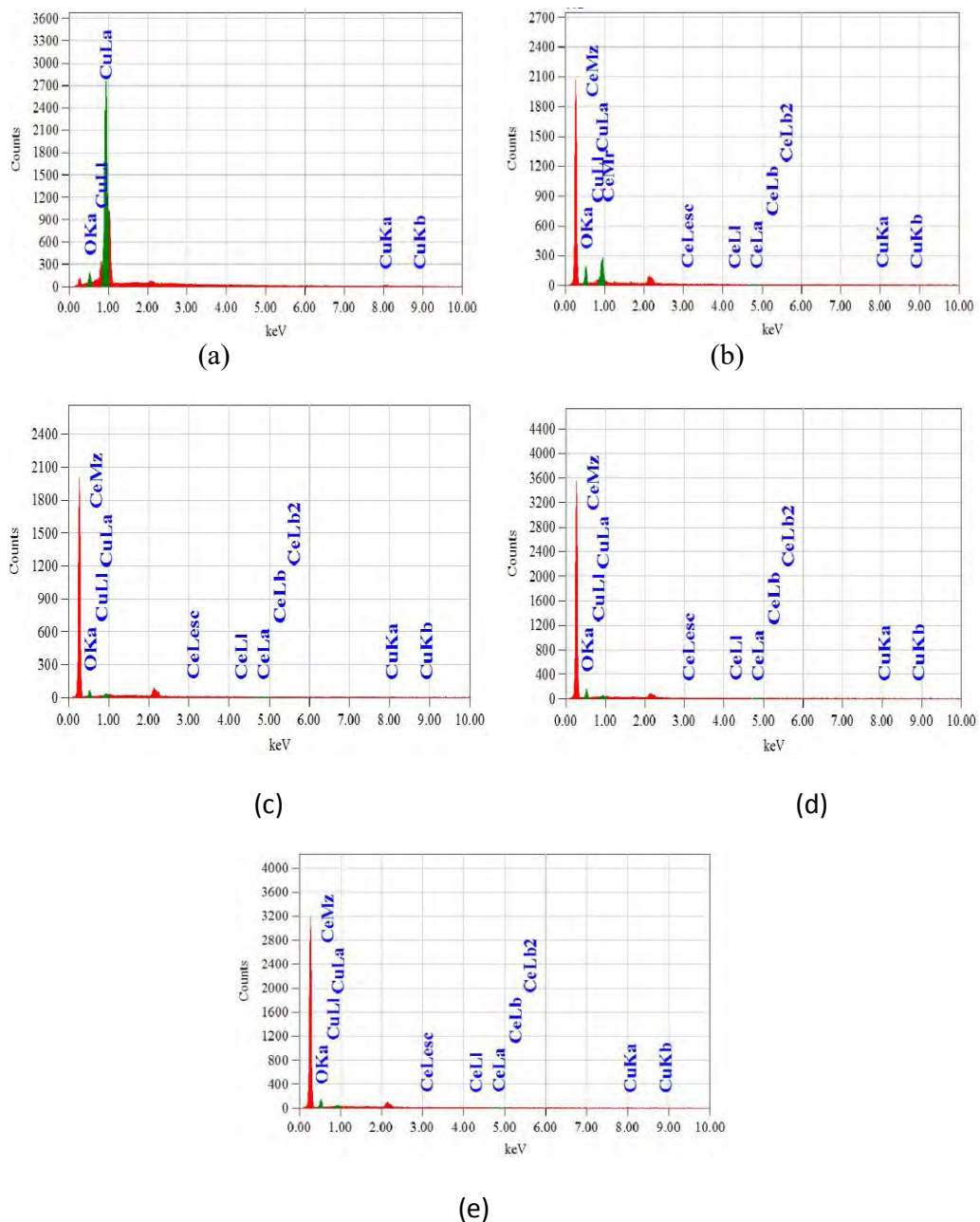


Fig. 23: EDS spectra of (a) pure CuO , (b) 2% Ce, (c) 4% Ce, (d) 6% Ce and (e) 8 mole% Ce doped CuO NPs.

4.3.1 Atom (%), mass (%), material presents in the samples

Table-3 is generated from EDS analysis of the samples while taking FESEM images. This table confirms the presence of Copper (Cu), Oxygen (O) and Cerium (Ce) in the corresponding samples. Besides XRD, confirmation of the particle can be known via EDS analysis.

Table 3: Material presence, atoms (%) and mass (%) of the pure CuO & Ce doped CuO NPs samples.

Samples	Materials	Mass (%)	Atom (%)
Pure CuO	Copper(Cu)	94	79.78
	Oxygen(O)	6	20.22
2 mole% Ce doped CuO	Copper(Cu)	58.03	26.63
	Oxygen(O)	40.05	72.97
	Cerium(Ce)	1.92	0.40
4 mole% Ce doped CuO	Copper(Cu)	20.53	7.53
	Oxygen(O)	61.41	89.47
	Cerium(Ce)	18.06	3.00
6 mole% Ce doped CuO	Copper(Cu)	15.52	4.89
	Oxygen(O)	74.95	93.75
	Cerium(Ce)	9.53	1.36
8 mole% Ce doped CuO	Copper(Cu)	10.27	2.96
	Oxygen(O)	84.02	96.29
	Cerium(Ce)	5.71	0.75

4.4 X-ray Diffraction (XRD)

The structural characteristics of the prepared samples have been investigated through XRD. In this part, the XRD patterns of pure CuO and Ce doped CuO samples are characterized that are discussed below.

4.4.1 Reitvelt analysis of pure and Ce doped CuO NPs

Reitvelt analysis [81] reveals almost every information of structural information of nanoparticles. It gives the phase of the structure, atomic positions in the structure, micro-strain, bond lengths between two neighboring atoms, bond angles and other necessary information for studying structural properties of nanoparticles. It also gives 3D structural information of the specific NPs. Here in this work Fullprof suite [82] software was used to study the CuO NPs by Reitvelt analysis.

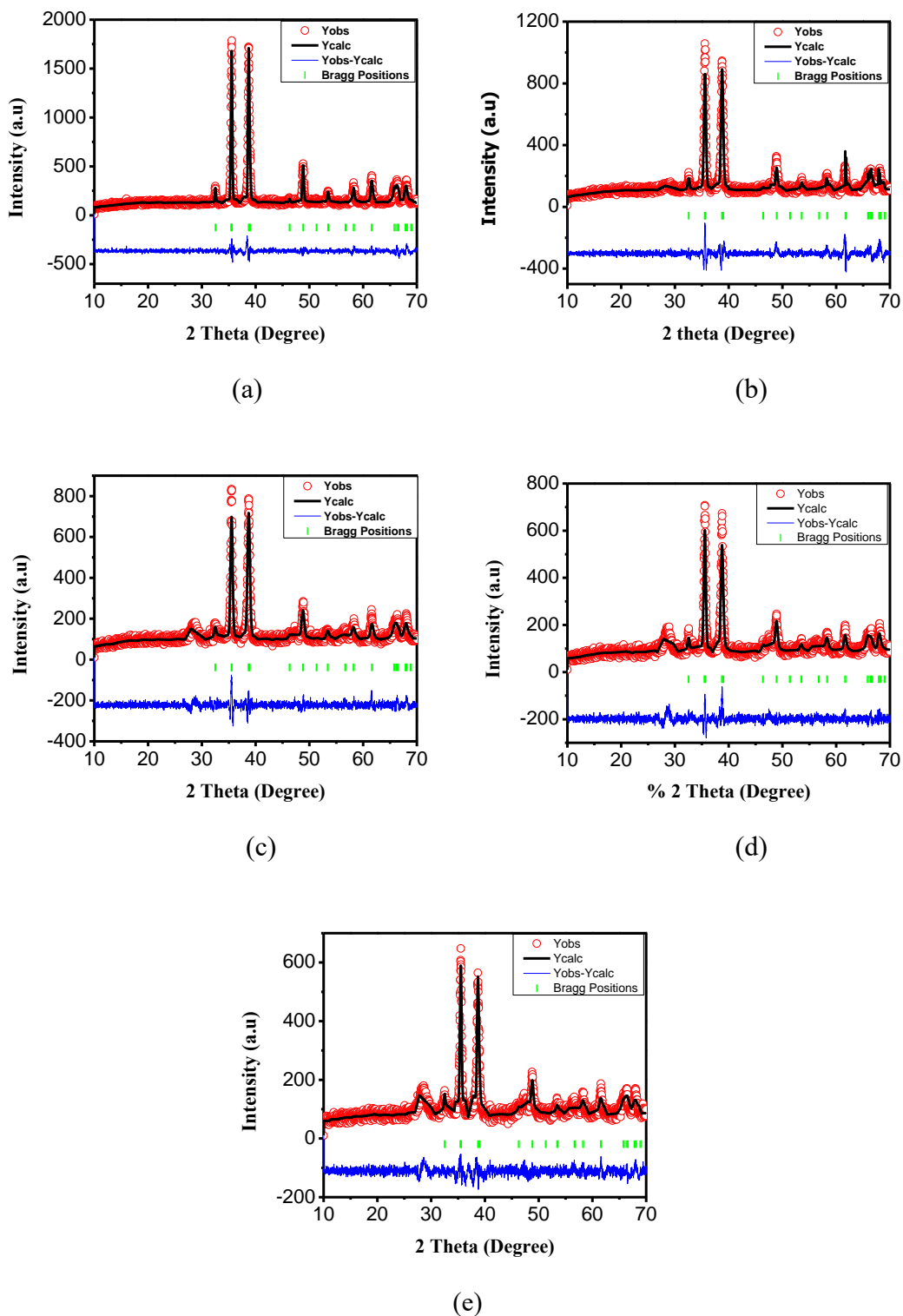


Fig. 24: Reitvelt analysis of (a) pure CuO NPs, (b) 2% Ce, (c) 4% Ce, (d) 6% Ce and (e) 8 mole% Ce doped CuO NPs.

4.4.2 3D structure of pure CuO and Ce doped CuO NPs

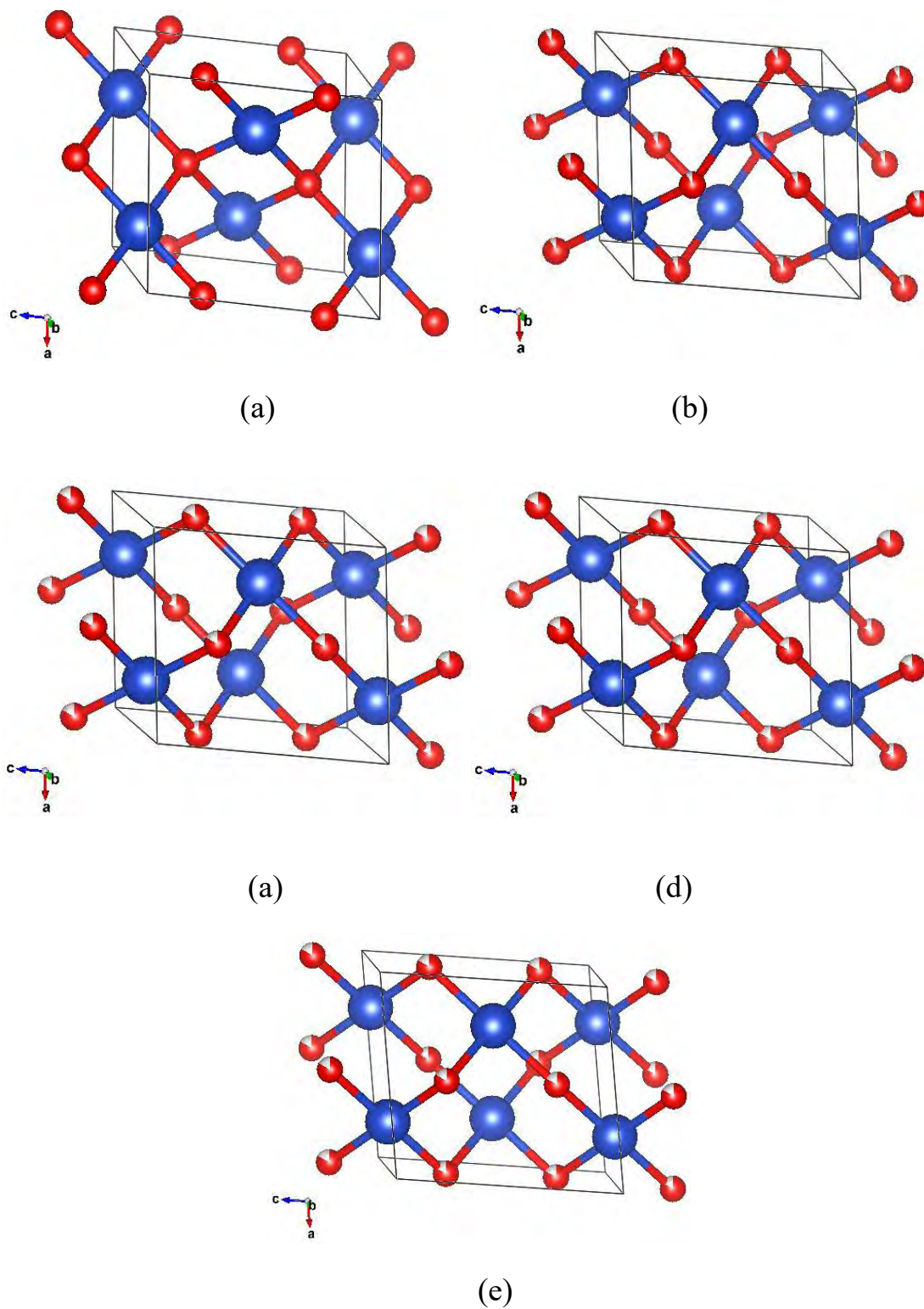


Fig. 25: Crystal structure of (a) pure CuO NPs, (b) 2% Ce, (c) 4% Ce, (d) 6% Ce and (e) 8 mole% Ce doped CuO NPs obtained by Reitvelt analysis.

After Reitvelt analysis we get a 3D structure of the CuO NPs. Now using VESTA [83] software, for pure CuO NPs, calculated Cu-O bond length 1.90455Å, Cu-Cu distance is 3.08401 Å & Cu-O-Cu bond angle is 104.38°. Variation of Cu-Cu bond length, Cu-O bond length or bond angle due to doping on CuO NPs can be analyzed by performing Reitvelt refinement. We can also calculate particles size, bond angle, bond length from Reitvelt refinement analysis of NPs. We can use these methods to study the structural effect of Ce NPs on CuO NPs.

4.4.4 XRD spectra of pure CuO & Ce doped CuO NPs

Figure 26 exhibits the XRD spectra of pure CuO and Ce doped CuO NPs. For analysis simplicity, XRD spectra of all samples were plotted in one graph. The XRD spectra of pure CuO NPs was plotted at the bottom of the graph and the Ce doped CuO NPs XRD were plotted vertically above the pure CuO NPs graph.

The diffraction peaks observed for the crystal planes (110), (-111), (111), (-202), (020), (202), (-113), (-311) and (220) at $2\theta = 32^\circ, 35^\circ, 38^\circ, 48^\circ, 53^\circ, 58^\circ, 61^\circ, 66^\circ$ and 68° confirmed the monoclinic crystalline planes of CuO [86]. The sharp diffraction peaks in the XRD patterns elucidate that CuO is highly crystalline in nature. However, the increasing of doping concentration of Ce levels decreases the intensity of diffraction peaks. The degrading of crystalline quality of CuO suggests that the increase of doping concentration deteriorates the crystal structure. In contrast with the undoped CuO a small peak was obtained at $2\theta = 28.5^\circ$ corresponding to (111) diffraction peak of CeO₂ [85] appears in Ce-doped CuO nanoparticles because of the doping of Ce ions. Moreover, by comparing XRD profiles between pure CuO NPs and Ce-doped CuO NPs, the diffraction peaks of Ce doped CuO NPs have a small shift (~ 0.31 degree) to higher angle. The atom radius of Ce⁴⁺ (87 pm) is larger than that of substituted Cu²⁺ (74 pm), which would be led to larger CuO lattice. According to Bragg diffraction equation that lattice constant is in proportion to d (interplanar distance), diffraction peaks will shift to smaller degree with increasing atom radius, indicating the incorporation of Ce ions into the CuO lattice. The XRD results also demonstrate that the synthesized NPs are the compound phase with CuO of a monoclinic structure and CeO₂ of a cubic structure. There are no impurity peaks except Ce element conspicuously in the XRD

patterns, so the samples are CuO of monoclinic structure and CeO₂ of cubic structure with high purity.

As Cu, O and Ce NPs presence has been confirmed already by XRD, we may look into more deeply through XRD analysis. We already showed our Reitvelt analysis result previously. Reitvelt analysis provides values of FWHM, d-spacing, peak position, peak center, relative intensity, particle size and so many info. These information helps to understand the doping effect of Ce NPs over CuO NPs. Such that: Changes of peak position to higher or lower 2 θ values due to doping effect, change of peak position, change of peak center, change of lattice parameters (a, b, c) etc.

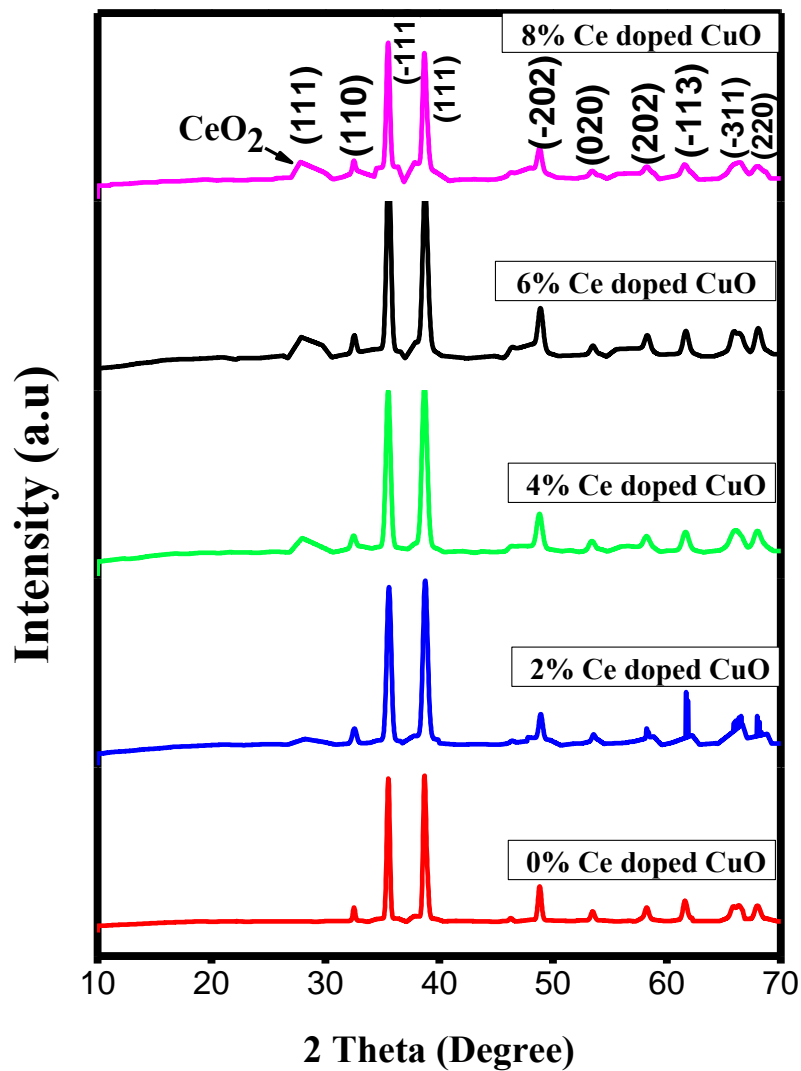


Fig. 26: Intensity distribution of Pure CuO and Ce doped CuO NPs.

There are several peaks in the XRD pattern. Every peaks shows similar tendency. As Ce is doped on CuO NPs, the position of peak change to higher or lower 2θ position depending on Ce concentration; peak center, FWHM, d-spacing also changes. If we study one single peak properly we don't need to analyze other peaks as all the peaks show same tendency. Besides, it is very difficult to study every peak in X-Ray diffraction pattern as well as this will give the same result.

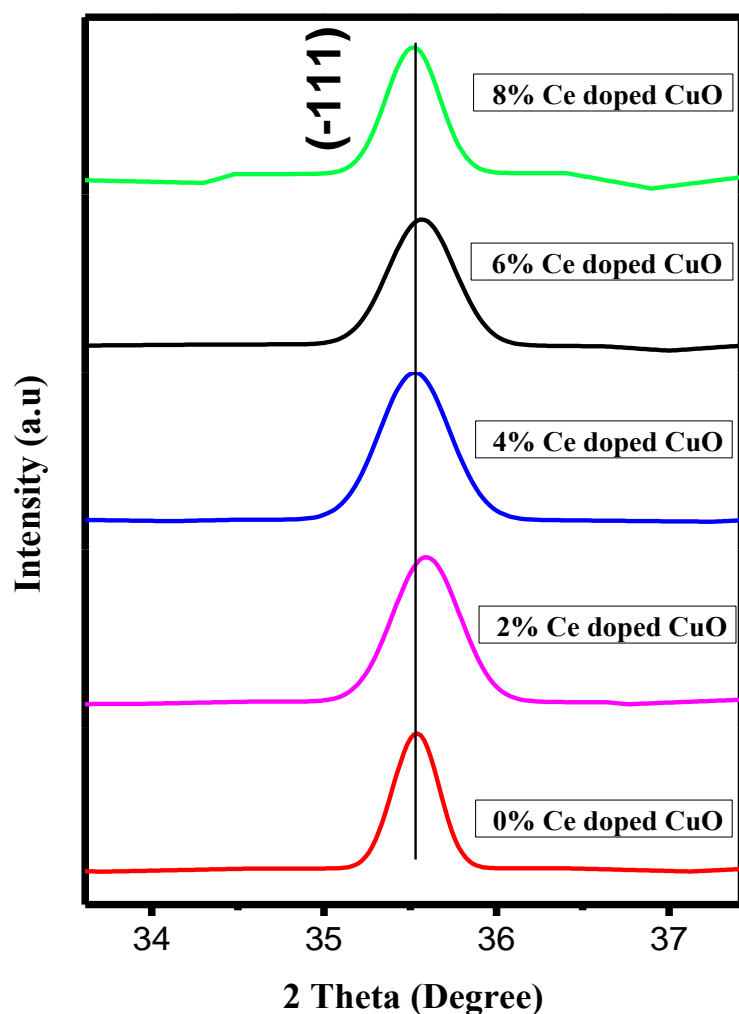


Fig. 27: Magnification of XRD pattern of (-111) plane

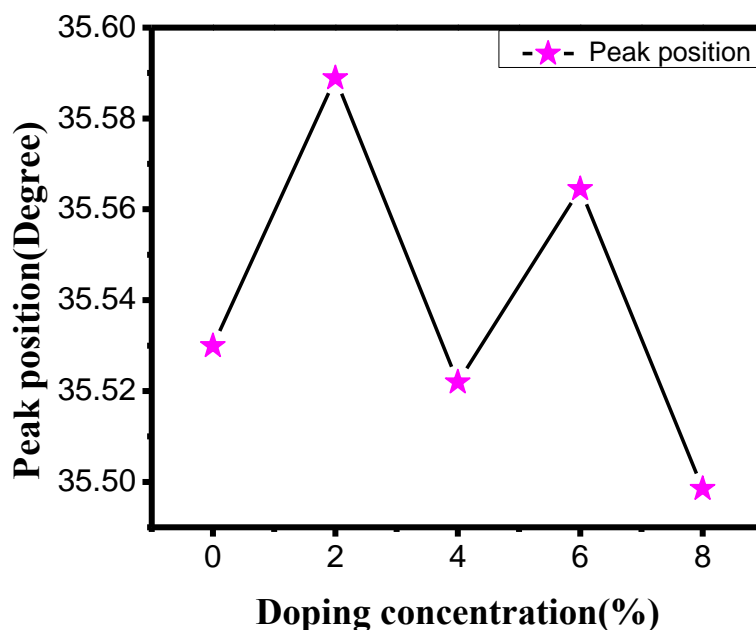


Fig. 28: Variation of peak position due to Ce doping on CuO NPs.

In our XRD analysis we study (-111) peak only as it is the dominant one. This peak has the highest intensity among all other peaks in the XRD spectra and this peak gives the value higher than one. So, this peak can be chosen to be analyzed.

The most interesting thing in the above figures is that when Ce NPs were added to pure CuO NPs, the peaks are moving to higher and lower 2θ position alternately. Fig. 27. This can be explained using lattice strain. Lattice strain may be originated from thermal or mechanical stress or any other sources of stress. Variation of bond length can also develop lattice strain. This lattice strain changes d-spacing. d-spacing may increase or decrease depending on lattice strain. The Bragg angle should either decrease or increase when d-spacing changes.

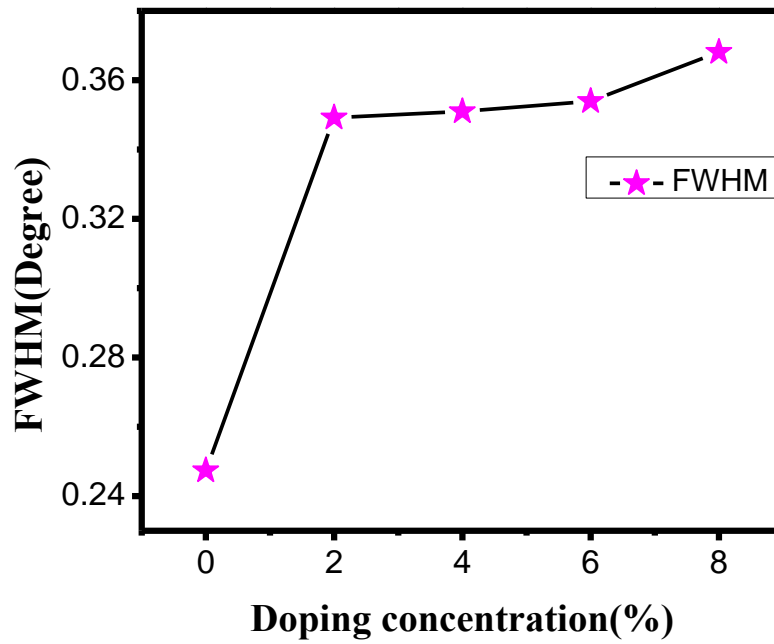


Fig. 29: Variation of FWHM of (-111) plane due to Ce doping on CuO NPs.

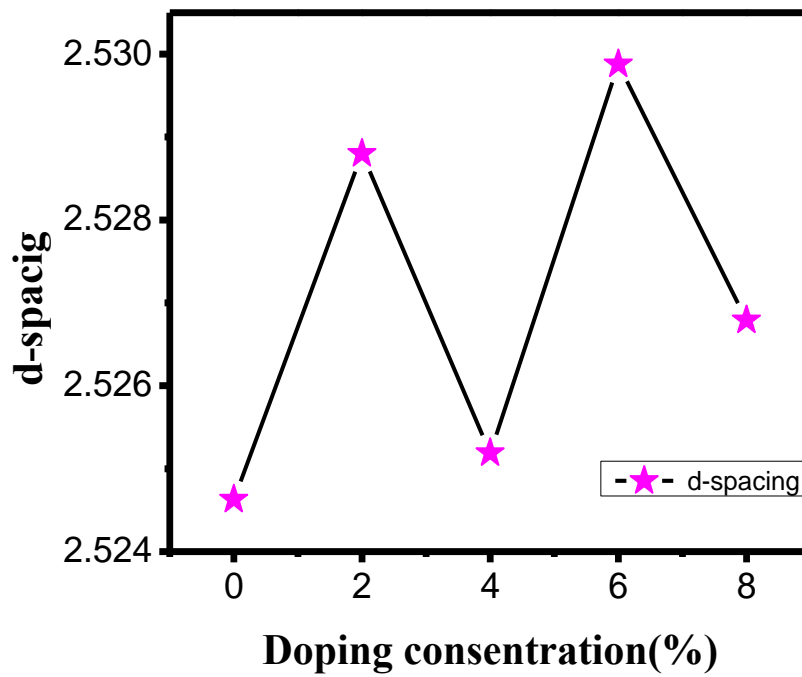


Fig. 30: Variation of of d-spacing due to Ce doping on CuO NPs.

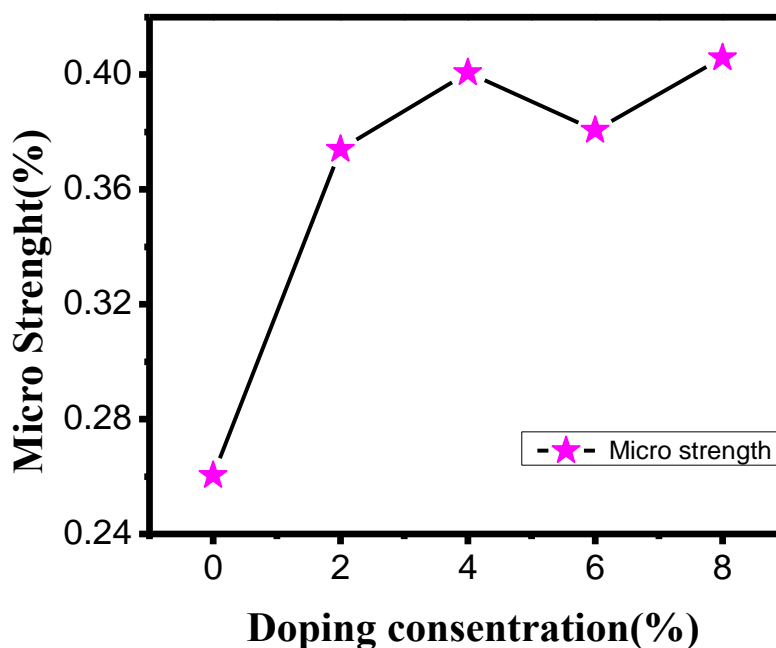


Fig. 30(b): Variation of micro strength due to Ce doping on CuO NPs.

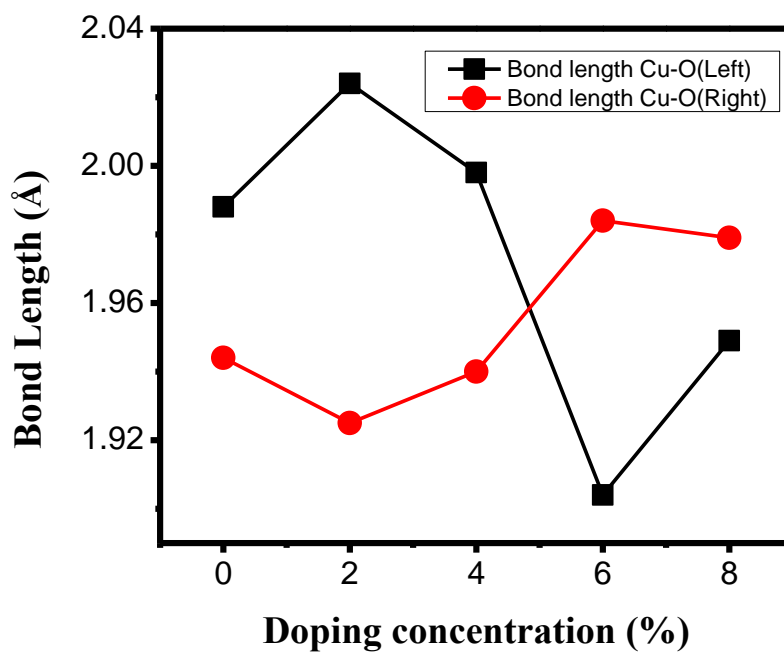
Thus, uniform compressive strain with decreasing the d -spacing shifts a Bragg's peak to higher 2θ value, whereas the uniform tensile strain with increasing the d -spacing shifts a Bragg's peak to lower 2θ value in the spectrum [12]. We say a uniform stress has been developed along (-111) plane. As d -spacing is increased while increasing Ce concentration, we consider a uniform strain (hence stress) has been created. Stress, strain can be calculated using various equations. Particle size can also be calculated at the same time.

4.4.5 Change of bond angle, bond length:

The angle Cu-O-Cu angle, Cu-Cu distance and bond length can be obtained using VESTA [83] software after performing Reitvelt refinement analysis. Table 4 shows the Angles, Cu-Cu distance and bond length obtained for various sample. A little change has been observed on Cu-O-Cu angle, Cu-O bond length and Cu-Cu distance when Ce was doped on CuO NPs. Variation of bond length, bond angle of Cu-Cu and Cu-O is plotted in Fig. 30 and bond angle at Fig.32

Table 4: Bond length and bond angle for CuO and Ce doped CuO NPs.

Samples	Bond length (Å) (Cu-O) [Left]	Bond length (Å) (Cu-O) [Right]	Bond angle (Degree)
0 mole% Ce doped CuO	1.944	1.988	84.85
2 mole% Ce doped CuO	1.925	2.024	85.5
4 mole% Ce doped CuO	1.9404	1.9980	84.866
6 mole% Ce doped CuO	1.9849	1.9041	83.5805
8 mole% Ce doped CuO	1.979	1.949	84.7

**Fig. 30: Variation of bond length of Cu-O (left) and Cu-O (right) of the prepared NPs**

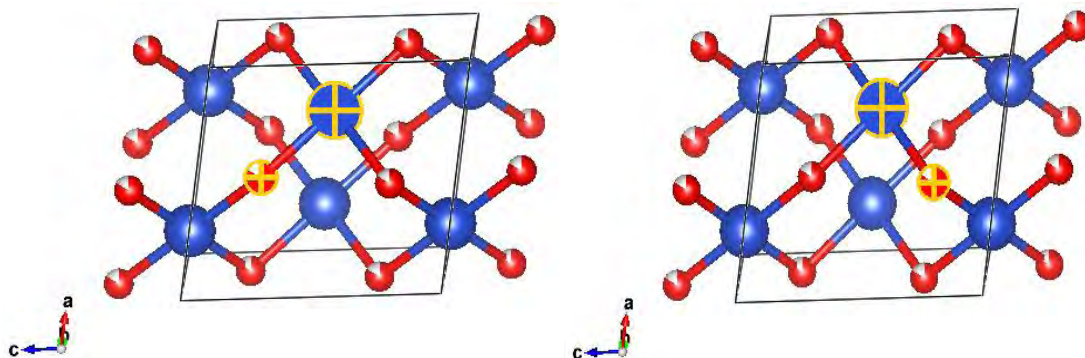


Fig. 31: Cu-O bond length (\AA) (red line) and Cu-Cu atomic distance (\AA) variation (black line) due to addition of Ce on CuO NPs.

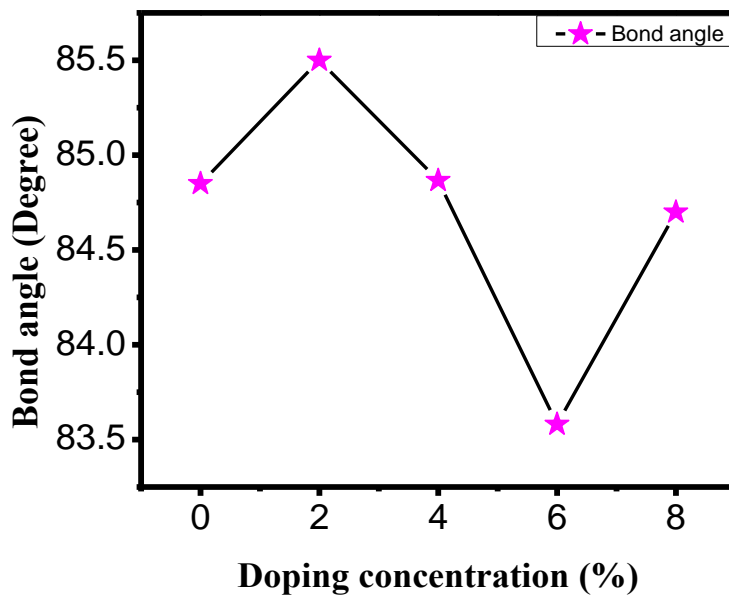


Fig. 32: Variation of bond angle due to Ce doping on CuO NPs.

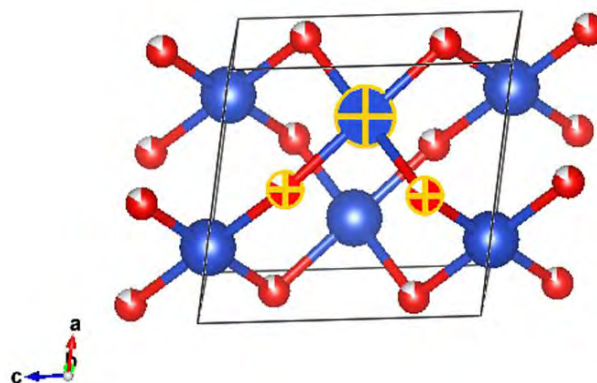


Fig. 33: O-Cu-O bond angle

As Ce NPs were added to CuO NPs, Cu-Cu atomic distance increases. The more Ce NPs are added, the more interatomic distance changes. If the bond length of left side of Cu-O bond increases, the right side of this Cu-O bond will decrease. But ultimately Cu-O bond of left side decreases and the Cu-O bond of the right-side increases while doping concentration of Ce was up to 8%. So, we can conclude that Ce NPs creates lattice strain on CuO [13]. As extra strain (also stress) is created, bond length and Cu-Cu distance changes. As bond length changes, bond angle also changes. Bond angles also shows increasing and decreasing tendency alternately. While 2 mole% Ce is doped the and angle of O-Cu-O increases, for 4 mole% and 6 mole% Ce doping the bond angle decrease and for 8 mole% Ce doping the bond angle again increase.

The variation of bond lengths develops the lattice strain [12]. Lattice strain also plays important role in crystal structure. Thermal stress or another source of strain like doping effect causes lattice contraction or lattice expansion [13]. Ce doping is responsible for changing lattice strain of CuO NPs.

4.4.6 Determination of particle size:

The crystallite size was estimated using the Scherer equation [40],

$$D = 0.9\lambda/(\beta\cos\theta)$$

Where,

λ is the wavelength of CuK α radiation,

θ is the Bragg diffraction angle of the peak and

β is the broadening of the diffraction line measured at half maximum intensity (FWHM) of the XRD peak.

Table 5: Change of particle size as a result of Ce doping on CuO NPs.

Samples	Particle size(nm)
Pure CuO NPs	20.64
2 mole% Ce doped CuO NPs	17.58
4 mole% Ce doped CuO NPs	15.48
6 mole% Ce doped CuO NPs	14.77
8 mole% Ce doped CuO NPs	14.66

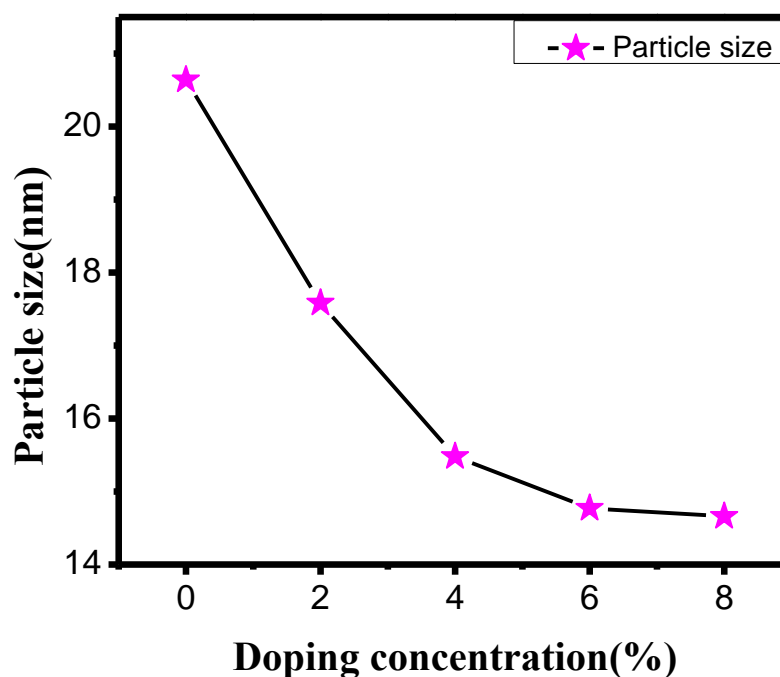


Fig. 34: Particle size variation pure and Ce doped CuO NPs

It is observed that the broadening of XRD peak of Ce doped samples indicate the reduction the size of CuO NPs. It can be seen that the specific surface area of Ce doped CuO is higher than the native CuO. This increase in surface area can be attributed to the decrease of the crystal size of the NPs. By applying the above formula for the broadening of (-111) peak reflection of CuO, the crystal sizes of pure CuO and Ce-doped CuO with different Ce doped concentrations samples were found to be 20.64 nm, 17.58 nm, 15.48 nm, 14.77 nm and 14.66 nm for Pure, 2 mole%, 4 mole%, 6 mole% and 8 mole% Ce doped respectively, indicating that doping with Ce creates surface defect sites and surface disorder, and had a depression effect on the growth of crystal size shown in Table 5 which might be due to the decrease in the crystallite size with increasing the Ce concentrations. It can be consisted with the results of FESEM. Thus, it is evident that the cerium amount influences significantly the surface area of photo catalysts.

4.5 FTIR analysis

In order to understand the chemical bonding and bond stretching nature of the synthesized CuO and the effect of the chemicals used in the synthesis of pure and Ce doped CuO NPs Fourier transform infrared (FTIR) spectroscopy analysis was carried out at room temperature in the range of (400–4000) cm^{-1} . Fig.35 shows the FTIR spectra of the pure CuO and different concentration of Ce doped CuO NPs.

The observed FTIR spectra exhibited various well-defined absorption bands at 487 cm^{-1} , 583 cm^{-1} , 682 cm^{-1} , 1101 cm^{-1} , 1627 cm^{-1} , 1658 cm^{-1} , 2373 cm^{-1} , 2926 cm^{-1} , 3452 cm^{-1} , 3705 cm^{-1} and 3774 cm^{-1} . The three peaks observed at 487 cm^{-1} , 583 cm^{-1} and 682 cm^{-1} are attributed to the characteristic stretching vibrations of metal–oxygen (Cu-O) bond in the monoclinic crystal structure of CuO. The absorption bands at 682 cm^{-1} and 583 cm^{-1} are attributed to the Cu-O stretching along the direction [-101] and the 487 cm^{-1} is attributed to the Cu-O stretching along the direction [101] [43]. No active bonds for Cu_2O or impurities were observed, thus indicating the formation of pure CuO sample from FTIR study.

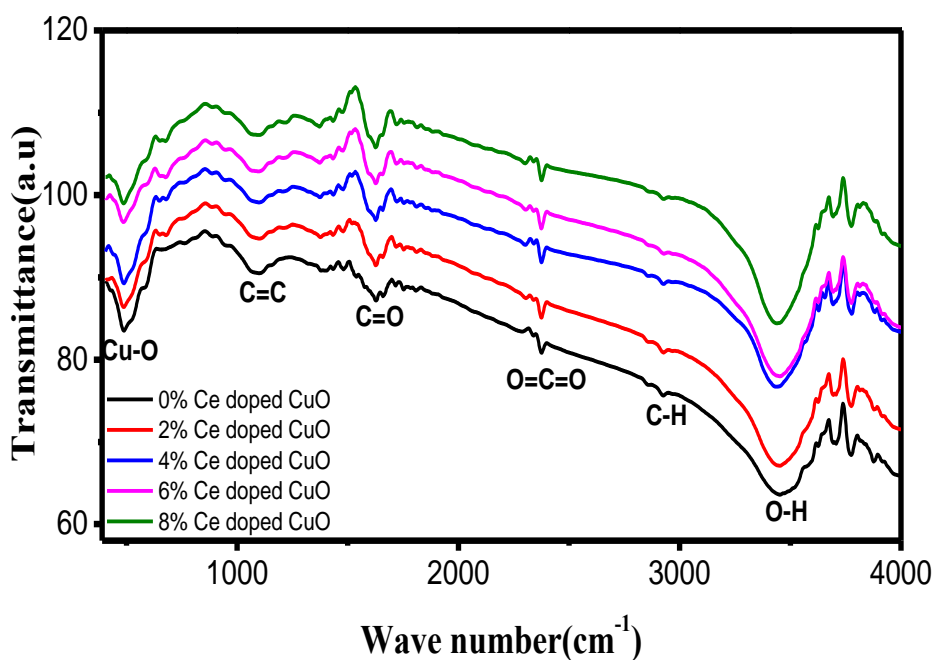


Fig. 35: FTIR spectra of pure CuO and Ce doped CuO NPs

The stretching vibration of carbonyl groups absorption band region is 1101 cm^{-1} - 1658 cm^{-1} . We found couple of peaks at 1101 cm^{-1} , 1627 cm^{-1} and 1658 cm^{-1} . These peaks may generate as a result of carbonyl group presented at citric acid. Stretching vibrations of C=C bonds are found in 1101 cm^{-1} . The peak 1658 cm^{-1} due to the C=O bond. The signal at 1627 cm^{-1} is associated with the molecular H₂O (H-O-H) bending frequency. The peak located at 2373 cm^{-1} is due to atmospheric CO₂ present in the instrument. Bands at 2926 cm^{-1} and 2860 cm^{-1} indicate to C-H stretching vibrations [1, 3, 4]. Strong wide band between (3500cm^{-1} - 3100 cm^{-1}) assigned to O-H stretching vibrations. This band is caused by presence of alcoholic and phenolic hydroxyl groups involved in hydrogen bonds. In our FTIR analysis we found a strong peak at 3452 cm^{-1} . We see four O-H bond which have come from citric acid. We also know that in demethylation process, one O-CH₃ bonds spited and CH₃ is replaced by a Hydrogen atom producing new OH group. When this process occurs, intensity of this band increases. We see two more peaks at 3693.68cm^{-1} and 3774.69 cm^{-1} in our analysis. These two peaks indicate that demethylation process may happen in our sample preparation process [1, 4]. No other absorption bands except those mentioned here are detected in the FTIR spectrum which substantiates that the synthesized NPs are almost pure without any significant impurity.

4.6 Raman Spectroscopy

In order to understand the structural and vibrational properties of the synthesized CuO and the effect of the chemicals used in the synthesis of CuO nanostructures at different doping concentrations, the Raman spectra of CuO nanostructures were obtained as shown in Fig. 36. CuO is a material with semiconducting properties that crystalline in a monoclinic structure has a space group symmetry of C_{2h}^6 ; the present study was performed to confirm the crystal structure of CuO nanostructures. The primitive cell contains two molecular units and thus there are twelve vibrational modes at the zone center including three acoustic modes (A_u+2B_u), six infrared active modes ($3A_u+3B_u$) and three Raman active modes (A_g+2B_g). These normal lattice vibrations at the Γ point of the Brillouin zone are given on the basis of group theory by the equation [24]: $\Gamma = (4A_u + 5B_u + A_g + 2B_g)$. Because of the site symmetry only oxygen atom displacements contribute to the Raman modes and thus the Cu atoms are stationary for these three modes where A_g mode is associated with in-phase/out phase rotation of the CuO, the B_{g1} associated with the bending of CuO, and the symmetric oxygen stretching mode corresponds to B_{g2} [88]. In standard single crystal CuO, an A_g Raman mode at 295 cm^{-1} and two B_g mode at 343 cm^{-1} and 615 cm^{-1} are usually observed [77].

The observed Raman spectra show change in the intensities and in number of modes which is attributed to the intrinsic defects. Here, the Raman spectrum of CuO samples synthesized at different doping concentrations with Ce shows the presence of all the three Raman active optical phonons ($A_g + 2B_g$) up to 6 mole%. With increase in the Ce doping level, it is found that the positions of the Raman peaks changes to the higher and lower wave number. For 4 mole% Ce and 6 mole% Ce doping the bands 295 cm^{-1} changes to 293 cm^{-1} , for 4 mole% Ce doping the bands 343 cm^{-1} changes to the higher wave number 345 cm^{-1} and the band 615 cm^{-1} doesn't change for Ce doping.

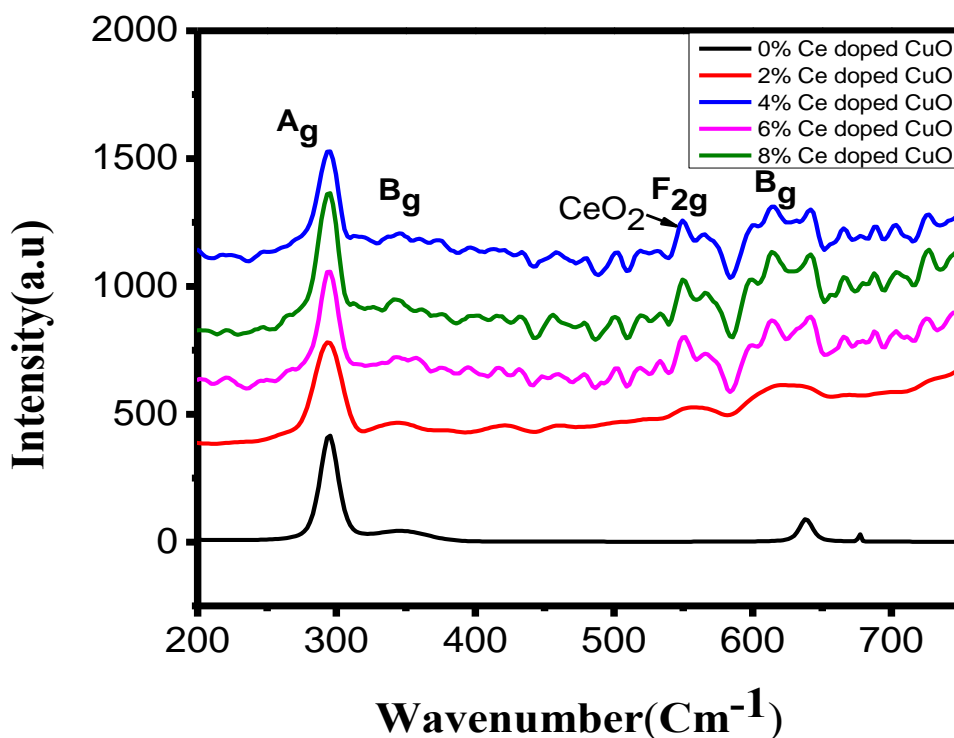


Fig. 36: Raman spectra of pure and Ce doped CuO NPs.

The Raman spectra of Ce doped CuO NPs confirms the presence of all the three characteristic Raman active modes of CuO up to 8 mole% Ce. In addition, we also observed a broader and relatively less intense for all three peaks at 295 cm^{-1} , 343 cm^{-1} and 615 cm^{-1} . The B_{g1} and B_{g2} almost vanishes due to the presence of Ce doping and it is caused due to the decreasing of particles size with increasing Ce doping. We also observed that CeO_2 belongs to $O5h$ ($Fm3m$) space group with cubic fluorite structure. The first order Raman line at around 549.42 cm^{-1} attributed to triply degenerate Raman active optical phonon mode (F_{2g}). The second order Raman spectrum, has nine phonon branches, with 45 possible. In this observation Raman spectrum of the CeO_2 nanoparticles with the fluorite phase measured a first order Raman peak (F_{2g}) at 453 cm^{-1} and there is no second order raman mode. These results are in good agreement with the XRD results.

4.7 Optical Properties

Semiconducting materials exhibit minimal optical absorption for photons with energies smaller than the band gap and high absorption for photons with energies greater than the band gap. As a result, there is a sharp increase in absorption at energies close to the band gap that manifests itself as an absorption edge in the UV-Vis absorbance spectrum.

While the absorption edge is indicative of the location of the band gap, accurate estimation of the band gap requires use of the following formula corresponding E_g (eV) values.

$$(\alpha h\nu)^2 = A(h\nu - E_g)$$

For direct band gap semiconductors: where α is the absorption coefficient, $h\nu$ is the energy of incident photons and E_g is the electronic band gap of the semiconductor. E_g is the intercept of the straight line obtained by plotting $(\alpha h\nu)^2$ vs $h\nu$.

It is known that the optical band gap energy of semiconductor materials may change with the size and shape of the particles or defects on the particles and also strongly dependent upon the synthesis methods used [26]. CuO is known to be a direct-allowed semiconductor material. A direct bandgap is a bandgap with direct transitions i.e. transitions where the energy changes (increases or decreases) but the momentum P i.e. the wave-vector k are conserved. For this reason, for a direct bandgap, the transitions are vertical. A direct bandgap is formed between the energy minimum of a highest band (e.g. conduction band) which occurs at the same value of the wave vector k as the energy maximum of a lower band (e.g. valence band). In our experiment, absorbance were plotted against wavelength, λ . The values of E_g can be obtained from extrapolating the straight-line portions of the curves $(\alpha h\nu)^2$ versus λ to the λ -axis (where $\alpha h\nu = 0$). There is a linear relationship between energy and wavelength as

$$E_g = h\nu/\lambda$$

Using this relation, we can calculate Energy band gap from Absorbance vs wavelength graph [2].

4.7.1 Band gap of CuO and Ce doped CuO NPs

Energy band gap was calculated from Absorbance versus wavelength graph separately for individual samples.

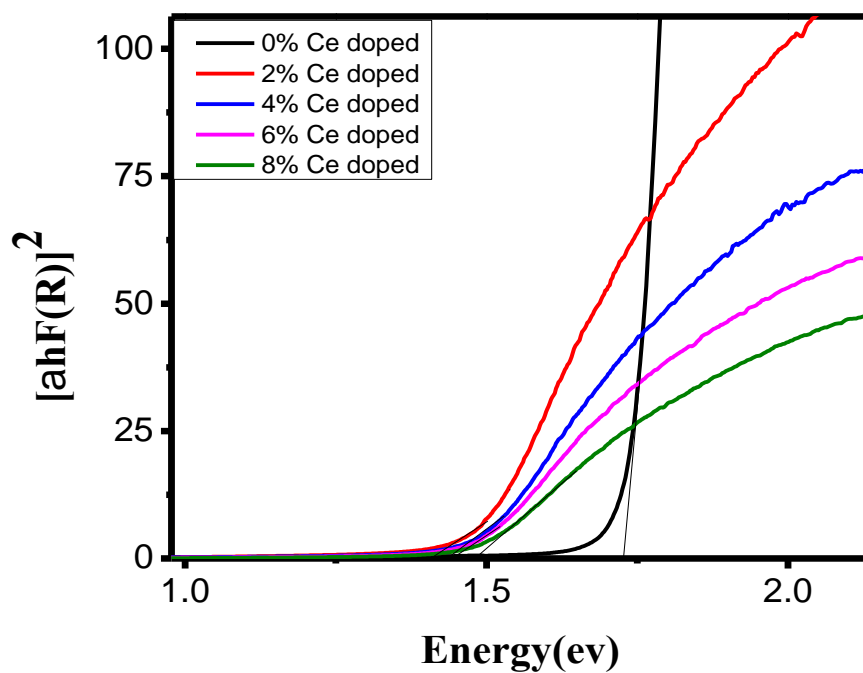


Fig. 37: Absorbance spectra of pure CuO & Ce doped CuO NPs.

4.7.2 Band gap of pure CuO & Ce doped CuO nanoparticles

Table 6: Change of band gap as a result of Ce NPs doping on CuO.

Samples	Energy band gap (eV)
0 mole% Ce doped CuO	1.72
2 mole% Ce doped CuO	1.40
4 mole% Ce doped CuO	1.42
6 mole% Ce doped CuO	1.44
8 mole% Ce doped CuO	1.48

4.7.3 Variation of optical band gap due to Ce doping

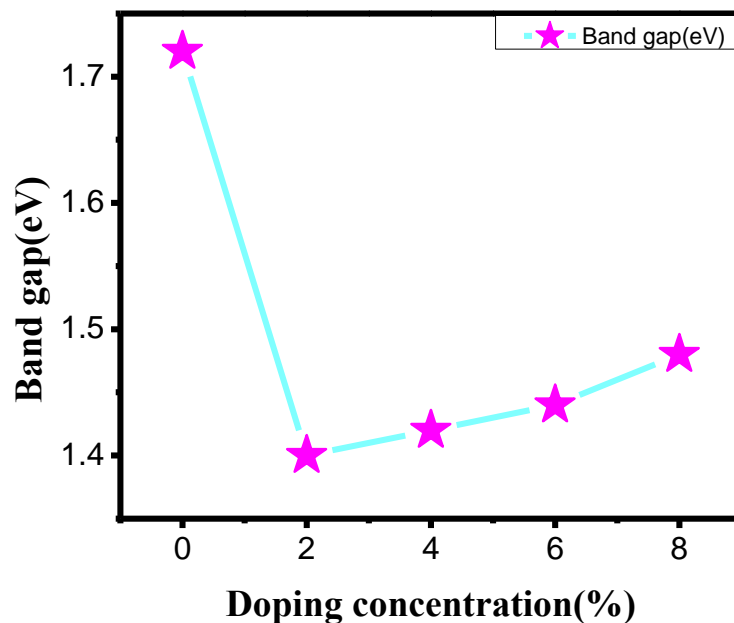


Fig. 38: Variation of energy gap due to doping of Ce NPs in pure CuO NPs.

In our sample band gap of pure CuO NPs is 1.72 eV which is near the CuO NPs band gap value 1.70 eV [22]. The band gap energy decreases with increasing Ce content in the sample. The reason may attribute to appearance of a new electronic state among the CuO band gap. The distance of charge transfer between f electrons of the Cerium ions and the conduction band (CB) or valence band (VB) of CuO is narrowed. Because of having the Ce^{4+} ion a 4f electron layer, the 4f layer helps to reduce the band gap energy of CuO samples [33].

When the doping amount of Ce is increased from 0 to 2 mole%, the absorbance intensity of the Ce doped CuO NPs increased in visible light region. It due to the fact that the Ce doped into the CuO crystal grains can greatly increase the visible light absorption ability. When the doping concentration increased from 4 mole% to 8 mole%, the visible light absorption ability of the Ce doped CuO is decreased. As we know, doping is usually accompanied by the formation of defects, which can play the role as trap centers to photoelectrons, but excessive doping may lead to some surface defects to act as the recombination centers for electron hole and thus increase the band gap for higher concentration of Ce doping. That is shown in the fig. 38 and table 6.

4.8 Photo-catalytic Activity of CuO and Ce Doped CuO NPs

Photo catalytic studies of pure CuO NPs and Ce doped CuO NPs as a photo catalyst have been examined by performing the photo degradation of methylene blue (MB) under the visible light irradiation. It was observed from the detailed photo catalytic experiments that the absorbance of MB dye solution decreases with increasing the illumination time. Moreover, with increasing the Ce doping concentration to 2 mole%, the degradation was increased significantly but further increasing the Ce doping concentration up to 8 mole% the degradation was decreased. The obtained results demonstrate that a particular amount of Ce doping (2 mole% Ce) into CuO is important to completely degrade the MB dye. Thus, at optimum Ce concentration (2 mole%), the prepared Ce doped CuO NPs are exhibiting appreciable photo catalytic degradation (99.5%) only within 60 min. Further, the Ce doped CuO NPs exhibited better photo catalytic performances compared to the CuO NPs. Fig. 40 exhibits the comparison bar diagram for the photo catalytic degradation of MB dye. Noticeably, the complete photo degradation was observed by different time for different samples. The percentage photo degradation increases with increasing the extent of Ce doping up to 2 mole% and afterward it decreases. Thus, it can be confirmed that 2 mole% Ce doping into CuO is the best composition for the complete degradation of MB dye in 30 min.

Fig.39 exhibits the variations of the absorbance vs wavelength as a function of visible light irradiation time for the photo catalytic degradation of MB dye in the presence of various Ce-doped CuO photo catalysts. A strong absorption band at wavelength 660 nm represents the λ_{max} for the dye under investigation. This band shows a steady decreasing trend for each Ce doped CuO photo catalyst with increasing irradiation times. The absorption maxima corresponding to the dye were decreasing; showing complete destruction of dye takes place in presence of the catalyst. It can also be clearly seen that almost complete photo degradation within 30 min of visible light irradiation is observed for 2 mole% Ce doped CuO photo catalyst for MB dye.

Fig.42 represents the percentage photo degradation of the MB dye with Ce concentration after 30 min of photo irradiation. It shows that the degradation rate increases from 53.93% for pure CuO to 98.64% for 2 mole% Ce doped CuO and then percentage photo degradation decreases to 82.41% for 8 mole% Ce doped CuO.

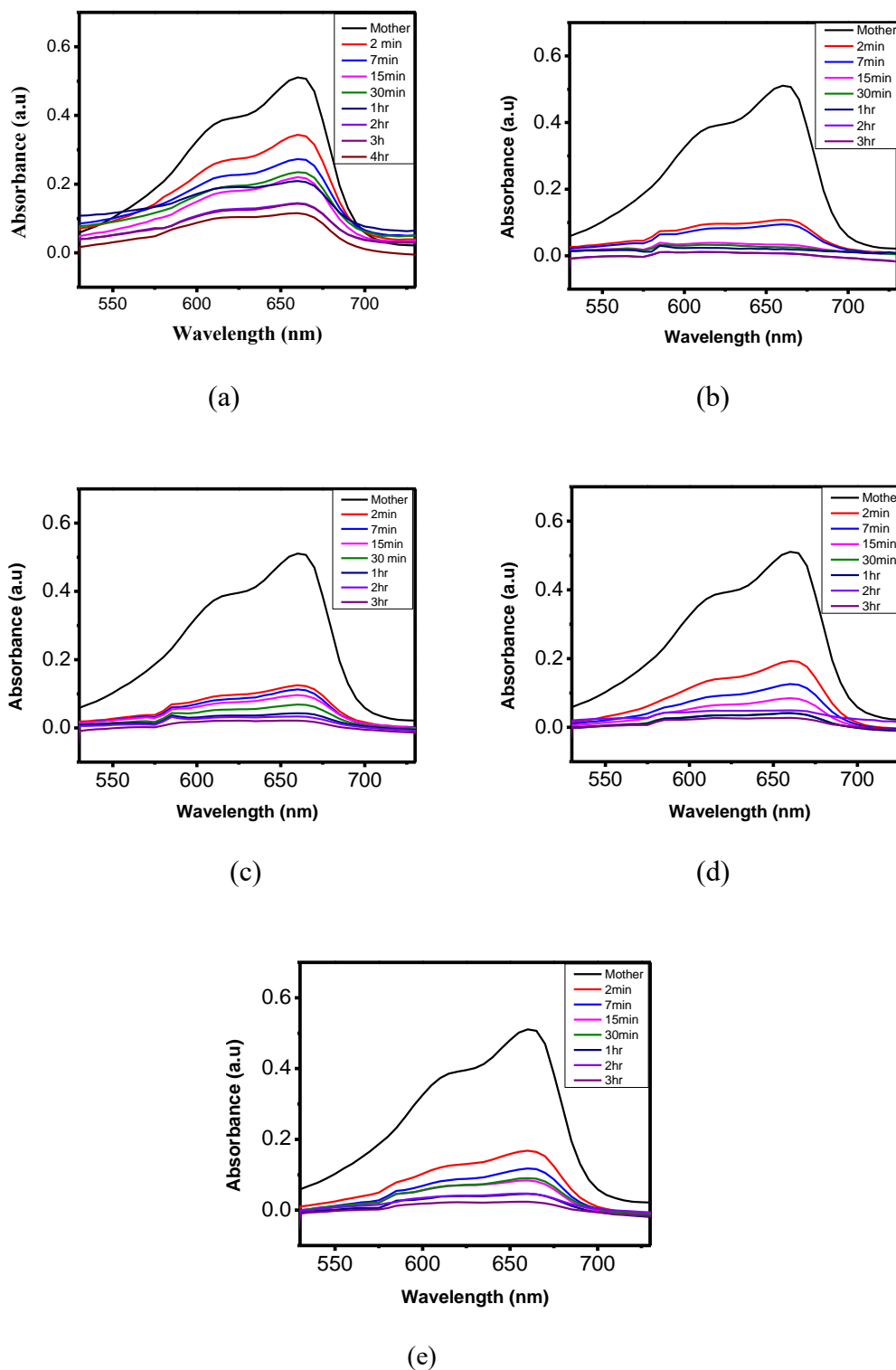


Fig. 39: The variation in UV–visible absorption spectra of methylene blue (MB) dye solution as a function of irradiation time in the presence of (a) pure CuO NPs, (b) 2 % Ce, (c) 4 % Ce, (d) 6 % Ce, (e) 8 mole% Ce doped CuO NPs as a catalyst under visible light illumination.

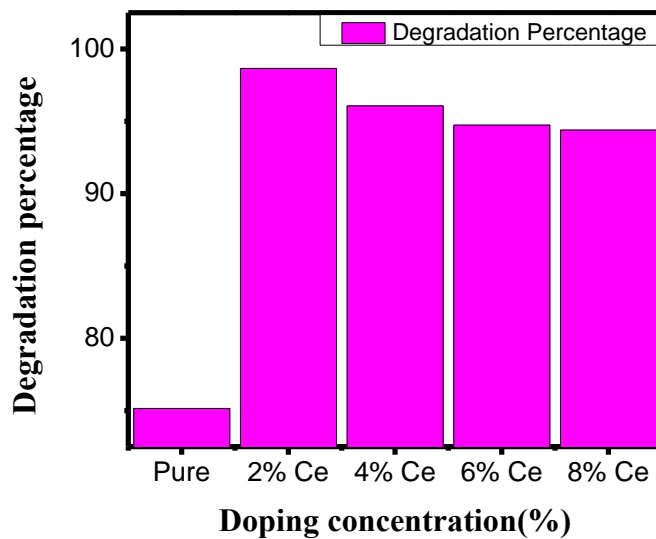


Fig. 40: Degradation percentage of MB dye for pure and Ce doped NPs.

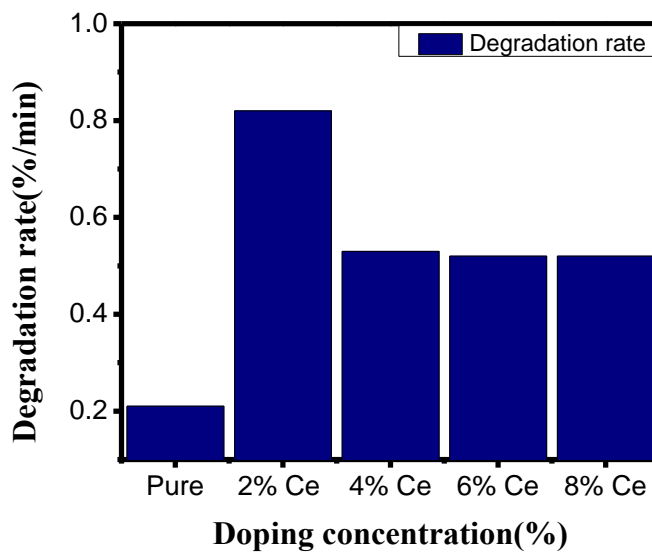


Fig. 41: Degradation rate of MB dye for pure and Ce doped CuO NPs.

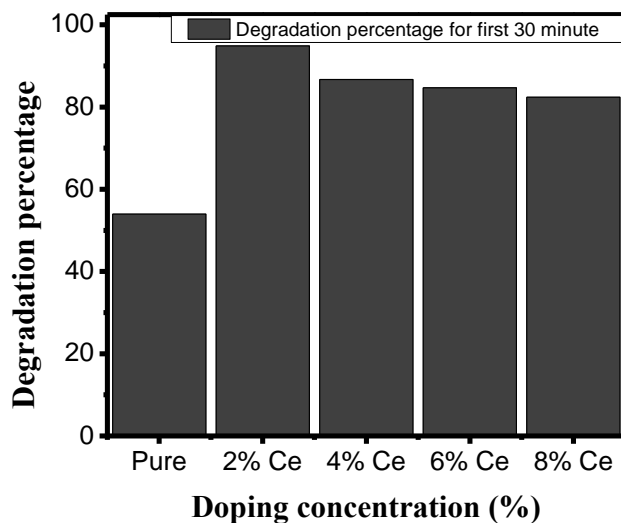


Fig. 42: Degradation percentage for first 30 minute of MB dye for pure and Ce doped CuO NPs.

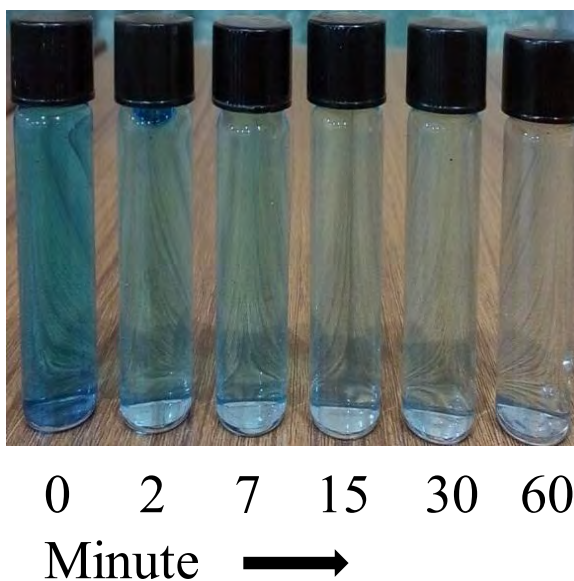


Fig. 43: Color change of the MB dye with prepared NPs under Visible light irradiation

4.8.1 Photo-catalytic mechanism

The enhanced photo catalytic activity of Ce doped CuO photo catalysts is explained on the basis of the electron and hole migration to the catalytic surface upon visible light irradiation and subsequent participation in redox reaction with the adsorbed dye.

Doping of Ce with CuO is expected to increase the surface defects, also refers to create trap centers, which enhance the photo catalytic efficiency. Ce^{4+} ions can also act as effective electron scavenger to trap the conduction band electrons, eliminating or reducing the probability of electron–hole recombination. This can efficiently transfer photo generated electrons to participate in redox reaction generating OH^- free radical causing dye degradation. Oxygen vacancy on the catalytic surface can also serve as trap for electrons from conduction band. But at higher Ce concentrations, the number of free electrons decrease as a result of the intrapping in Ce^{4+} ions, thereby decreasing photo-degradation [61].

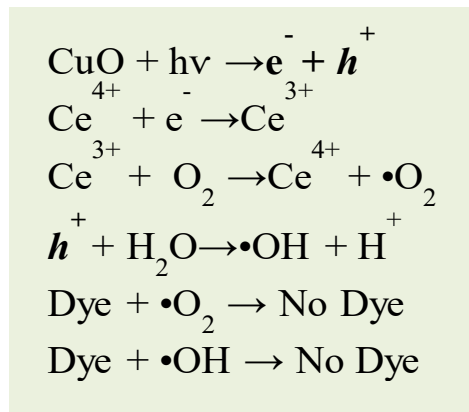


Fig. 44: Equation of photo-catalytic mechanism

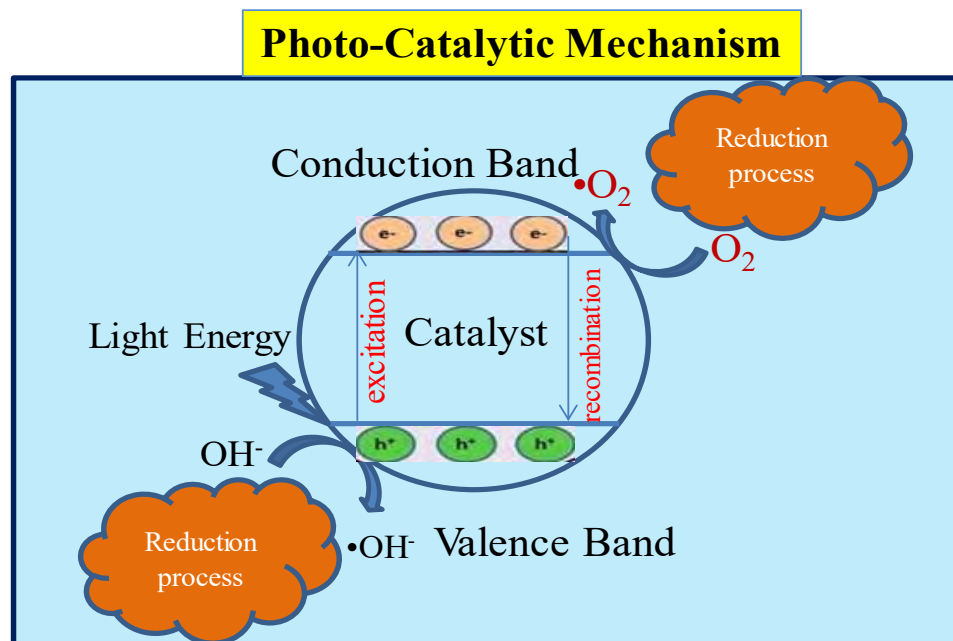


Fig. 45: Photo-catalytic mechanism

The proposed mechanism for the photo catalytic activity of Ce doped CuO is shown in Fig. 45 For Ce doped CuO NPs, the Ce^{4+} ions incorporated in CuO lattice are supposed to absorb photo-excited electrons from the conduction band of the CuO and get reduced into Ce^{3+} ions. Reduced Ce^{3+} ions are oxidized by transferring the electron to the adsorbed O_2 molecules which produce the superoxide radical (O_2^-) [65, 66]. As a result, a continuous trapping system becomes functional on the surface of the doped CuO nanoparticles and inhibits the electron-hole recombination. This means that Ce^{4+} on the surface of CuO nanoparticles may act as an electron scavenger. The O_2^- radical anions further result in the formation of HO^- radicals which are mainly responsible for the dye degradation.

Fig. 40 clearly presents that the prepared Ce doped CuO NPs photo catalysts exhibited better photo catalytic performances.

CHAPTER 5

CONCLUSION

5.1 Conclusion

In this present study CuO and Ce doped CuO NPs were successfully synthesized by a cost-effective, simple sol-gel auto-combustion process. Sol-Gel process offers a number of advantages including, low processing temperature, ability to control the composition on molecular scale and the porosity to obtain high surface area materials, homogeneity of the final product up to atomic scale, doesn't require annealing, thus energy and cost efficient.

The surface morphology of the NPs was observed by field emission scanning electron microscope (FESEM) was also performed to study the surface morphology of the nanoparticles. The FESEM images reveal that Ce doping reduces the size of the nanoparticles. EDS (Energy Dispersive Spectroscopy) analysis was also performed which confirm the presence of Cu, O, Ce in the samples.

The X-ray Diffraction patterns were to characterize the crystal structure of the CuO and Ce doped CuO NPs. Reitvelt analysis was performed to reveal the structural information of the nanoparticles. The effect of Ce doping on the different structural parameter such as lattice type, bond length, bond angles and reason behind the change of lattice parameter, strain and stress was studied in details.

FTIR analysis was also performed to know the components present in the prepared samples. Presence of Cu and O bond can be confirmed by FTIR. No active bonds are found for Cu₂O or impurities (Ce) in the prepared samples. Raman spectroscopy of the Ce doped CuO nanoparticle shows a change in the intensities and number of modes which is attributed to the presence of intrinsic defects.

Optical properties of the NPs were investigated by a UV-Visible Spectroscopy. The optical band gap of the CuO and Ce doped CuO NPs were evaluated from the optical data. It was found the 2 mole% Ce doping reduces the band gap of CuO NPs from 1.72 eV to 1.40 eV. Due to having the Ce⁴⁺ ion a 4f electron layer, the 4f layer helps to reduce the band gap energy of CuO samples. A further increase in Ce dopant enhances the band gap but it is far less than the band gap of pure CuO. Excessive doping of Ce may lead to some surface defects to act as the recombination centers for electron hole and thus increase the band gap for higher concentration of Ce doping.

Photo-catalytic studies of pure CuO NPs and Ce-doped CuO NPs as a photo-catalyst have been examined by performing the photo degradation of methylene blue (MB) under the visible light irradiation. The Photo-catalytic studies showed that Ce doping improves the photo-catalytic activity of CuO Nps. 2 mole% Ce doped CuO NPs yields the best photo-catalytic activity. The photo-catalytic activity reduces with the increase of dopant concentration. The higher surface area of the NPs due to smaller particle size distribution together with its lower band gap is responsible for the enhanced photo-catalytic activity of Ce doped CuO than the pure CuO NPs. The Ce doped CuO NPs synthesized by an effective and economic route may open up a versatile route to enhance the photo-catalytic activity of CuO NPs and can find their applications in water purification and environment cleaning.

5.2 Suggestions for the Future Work

In order to better understand the role of Ce doping on the physical properties of CuO nanoparticle several studies can be performed. Additionally, studies can be done to explore the potential application of these nanoparticles. A list of suggestion for the possible future works is given below:

1. Analyze the Photoluminescence spectra of CuO and Ce doped CuO NPs
2. Study the dielectric property of pure CuO and Ce doped CuO NPs.
3. A Study the effect of Ce doping on the antibacterial property of CuO NPs.
4. Theoretical structural analysis, DFT can be performed then compare with the experimental result

CHAPTER 6

REFERENCES

Reference

- [1] Monaliben, S., Derek, F., Shashi, S., Suraj, K. T., G errard E. J. P., "Green synthesis of metallic nanoparticles via biological entities," *Mater. Sci.*, vol. 8, pp. 7278–7308, 2015.
- [2] Gregory, G., Sergio, M., Francis, L. D., "Nanomaterial properties: size and shape dependencies," *J. Nanomater.*, vol. 2012, pp. 2, 2012.
- [3] Francois, F., Ludovic, E., Gerard, B., "Optical properties of nanostructured materials: a review," *J. Nanophotonics*, vol. 5, pp. 1934-2608, 2011.
- [4] Attarad, A., Hira, Z., Muhammad, Z., Ihsan-ul H., Abdul R. P., Joham S. A., Altaf H., "Synthesis, characterization, applications, and challenges of iron oxide nanoparticles," *Nanotechnol. Sci. Appl.*, vol. 9, pp. 49-57, 2016.
- [5] Jiri, K., Yazan, H., Lukas, R., Zbynek, H., Mirko, C., Vojtech, A., Ondrej, Z., "Magnetic nanoparticles: From design and synthesis to real world applications," *J. Nanomater.*, vol. 7, pp. 243-273, 2017.
- [6] Wang, Hui., Xu, J.Z., Zhu, J.J., Chen, H.Y., "Preparation of CuO nanoparticles by microwave irradiation", *J. Cryst. Growth*, vol. 244, pp. 88-94, 2002.
- [7] Ibrahim, K., Khalid, S., Idrees, K., "Nanoparticles: Properties, applications and toxicities," *J. Chem.*, vol. 16, pp. 262-271, 2017.
- [8] Hyeong, C. J., Ellen, D. W., "Steps on surfaces: experiment and theory," *Surf. Sci. Rep.*, vol. 34, pp. 171-294, 1999.
- [9] Wei, W., Zhaohui, W., Taekyung, Y., Changzhong, J., Woo, S. K., "Recent progress on magnetic iron oxide nanoparticles: synthesis, surface functional strategies and biomedical applications," *Sci. Technol. Adv. Mater.*, vol. 16, pp. 43-87, 2015.
- [10] Pankhurst, Q. A., Connolly, J., Jones, S. K., Dobson, J., "Applications of magnetic nanoparticles in biomedicine," *J. Phys. D: Appl. Phys.*, vol. 36, pp. 167-181, 2003.
- [11] Lodhia, J., Mandarano, G., Ferris, N. J., Eu, P., Cowell, S. F., "Development and use of iron oxide nanoparticles (Part 1)," *Biomed. Imaging Interv. J.*, vol. 2, pp. 6-17, 2010.

- [12] Vidyasagar, C.C., Arthoba Naik, Y., Venkatesha, T.G., Viswanatha,R., ‘*Nano Micro Letter.*’ Vol. 4, pp. 73–77. 2012.
- [13] Ruohong, S., Paul, C., "Synthesis of metal oxide nanostructures by direct Sol–Gel chemistry in supercritical fluids," *Chem. Rev.*, vol. 112, pp. 3057–3082, 2012
- [14] Khalil, M.I., "Co-precipitation in aqueous solution synthesis of magnetite nanoparticles using iron (III) salts as precursors," *Arab. J. Chem.*, vol. 8, pp. 279–284, 2015.
- [15] Amir, H. R., Mohammad, R. V., Ali S., Zohreh, R., "Synthesis of iron oxide nanoparticles via sonochemical method and their characterization," *Particuology*, vol. 9, pp. 95–99, 2011.
- [16] Jianlin, L., Qingliu, W., Ji, W., "Synthesis of nanoparticles via solvothermal and hydrothermal methods," *Handbook of Nanoparticles*, vol. 17, pp. 295–328, 2015.
- [17] Markus, N., Georg, G., Jelena,B., Julien, P., Jianhua, B., Nicola, P., "Nonaqueous synthesis of metal oxide nanoparticles:Review and indium oxide as case study for the dependence of particle morphology on precursors and solvents," *J. Sol-Gel Sci. Techn.*, vol. 40, pp. 259–266, 2006.
- [18] Garciaa, M. I. D., Orezza, V. M., Jankulovskaa, M., Anandanb, S., Bonetea, P., Gomez, R., Villarreal, T. L., "Effects of ultrasound irradiation on the synthesis of metal oxide nanostructures," *Phys. Procedia*, vol. 63, pp. 85 – 90, 2015.
- [19] Maqsood, A. M., Mohammad, Y. W., Mohd, A. H., "Microemulsion method: A novel route to synthesise organic and inorganic nanomaterials," *Arab. J. Chem.*, vol. 5, pp. 397–417, 2012.
- [20] Vidyasagar, C.C., Arthoba Naik, Y., Venkatesha, T.G., Viswanatha,R., ‘*Nano Micro Letter.*’ Vol. 4, pp. 73–77. 2012.
- [21] Volanti, D.P., Keyson, D., Cavalcante, L.S., Simoes, A.Z., Joya, M.R., Longo, E., Varela, J.A., Pizani, P.S., Souza, A.G., “*Journal of Alloys and Compound*”. Vol. 459, pp. 537–542, 2008.
- [22] Xu, D., Zhang, M., Feng, J., Zhang, M.L., “*Material Letter*”. Vol. 62 pp. 2787–2790, 2008.

- [23] Li, Y., Kuai, P., Huo, P., Liu, C., “*Material Letter*”. Vol. 63, pp. 188–190, 2009.
- [24] Jiang, T., Wang, Y., Meng, D., Wu, X., Wang, J., Chen, J., “Controllable fabrication of CuO nanostructure by hydrothermal method and its properties”. *Apl. Surf. Sci.*, vol. 311, pp. 602–608, 2014.
- [25] Zhang, X.J., Zhang, D.G., Ni, X.M., Song, J.M., Zheng, H.G., “*Journal of Nanoparticle*”. Vol. 10, pp. 839–844, 2008.
- [26] Niasari, M.S., Davar, F., “*Material Letter*”. Vol. 63, pp. 441–443, 2009.
- [27] Makarov, V. V., Love, A. J., Sinitsyna, O. V., Makarova, S. S., Yaminsky, I. V., Taliansky, M. E., Kalinina, N. O., "Green nanotechnologies: synthesis of metal nanoparticles using plants," *Acta Naturae*, vol. 6, pp. 35–44, 2014.
- [28] Sadia, S., Arifa, T., Yongsheng, C., "Green synthesis of iron nanoparticles and their environmental applications and implications," *Nanomaterials*, vol. 6, pp. 209-235, 2016.
- [29] Nazari, A., Riahi, S., “*Sadhana-Acad. Proc. Eng. Sci*”. vol. 36, pp. 371–391, 2011.
- [30] Egan, G.C., Sullivan, K.T., Olson, T.Y., Han, T.Y., Worsley, M.A., Zachariah, M.R., “Ignition and combustion characteristics of nanoaluminum with copper oxide nanoparticles of different oxidation state”. *The Journal of Physical Chemistry*, vol. 120(51) pp. 29023-29029, 2016.
- [31] Max, B., "The use and meaning of nano in American English: Towards a systematic description," *Ampersand*, vol. 3, pp. 163-173, 2016.
- [32] Richard, P. F., "There's plenty of room at the bottom," *Appl. Magn. Reson.*, vol. 24, pp. 890-905, 1959.
- [33] Mansoori, G. A., Soelaiman, T. A. F., "Nanotechnology-an introduction for the standards community," *J. ASTM Int.*, vol. 2, pp. 428-448, 2005.
- [34] Roco, M.C., "The vision and action plan of the national nanotechnology initiative." *Nanotech.* vol. 2, pp. 1-5, 2002.
- [35] Ruth, L., "Information resources in toxicology," *Adv. Mater.*, vol. 4, pp. 321-328, 2009.

- [36] Jaison, J., Ahmed, B., Yen, S. C., Alain, D., Michael, K. D., "Review on nanoparticles and nanostructured materials: history, sources, toxicity and regulations," *Beilstein J. Nanotechnol.*, vol. 9, pp. 1050–1074, 2018.
- [37] Khalid, M. A., Salman, A. A., Muhammad, N. K., Anees, A. A., "Nanomaterials as analytical tools for genosensors," *J. Sens. Sci. Technol.*, vol. 10, pp. 963-993, 2010.
- [38] Megan, E. M. Melissa, J. P., "Are nanoparticles potential male reproductive toxicants? A literature review," *Nanotoxicology*, vol. 1, pp. 204210, 2007.
- [39] Tarafdar, J. C., Shikha, S. Ramesh, R., "Nanotechnology: Interdisciplinary science of applications," *Afr. J. Biotechnol.*, vol. 12, pp. 219-226, 2013.
- [40] Emil, R., "Size matters: why nanomaterials are different," *Chem. Soc. Rev.*, vol. 35, pp. 583–592, 2006.
- [41] Andrew, M. S., Shuming, N., "Semiconductor nanocrystals: structure, properties, and band gap engineering," *J. Am. Chem. Soc.*, vol. 43, pp. 190-200, 2010.
- [42] Sagadevan, S., "Semiconductor nanomaterials, methods and applications: A review," *J. Nanosci. Nanotechnol.*, vol. 3, pp. 62-74, 2013.
- [43] Robert. P., Martina, T., "Designing drugs that overcome antibacterial resistance: where do we stand and what should we do?" *Expert Opin. Drug Discov.*, vol. 10, pp. 631-650, 2015.
- [44] Xi, Z., Aleksandar, F. R., Jun, W., Robert, L., Jinjun, S., "Nanomedicine in the management of microbial infection-Overview and perspectives," *Nano Today*, vol. 9, pp. 478–498, 2014.
- [45] Linlin, W., Chen, H., Longquan, S., "The antimicrobial activity of nanoparticles: present situation and prospects for the future," *Int. J. Nanomedicine*, vol. 12, pp. 1227–1249, 2017
- [46] Zhou, F., Zhou, R., Hao, X., Wu, X., Raw, W., Chen, Y., Gao, D., "Influences of surfactant (PVA) concentration and pH on the preparation of copper nanoparticles by electron beam irradiation". *Radiation Physics and Chemistry*, vol. 77, pp. 169–173, 2008.
- [47] Bolla, G. R., Deboshree, M., Benjaram, M .R. "Novel approaches for preparation of nanoparticles," *J. Nanostruct.*, vol. 19, pp. 1-36, 2017.

- [48] Ying, J. Z., Feng, C., "Microwave-assisted preparation of inorganic nanostructures in liquid phase," *Nano Lett.*, vol. 14, pp. 6462–6555, 2014.
- [49] Yujun, S., "Hot wire chemical vapor deposition chemistry in the gas phase on the catalyst surface with organosilicon compounds," *Acc. Chem. Res.*, vol. 48, pp. 163–173, 2015.
- [50] Cristina, L., Sridhar, K., "Inorganic syntheses assisted by microwave heating," *Inorganics*, vol. 3, pp. 388-391, 2015.
- [51] Sarah, C. M., Sreejarani, K. P., Suprakas, S. R., Kalala, J., Rui, W. M. K., "Recent trends in the microwave-assisted synthesis of metal oxide nanoparticles supported on carbon nanotubes and their applications," *J. Nanomater.*, vol. 69, pp. 1-15, 2012.
- [52] Alexander, S. M., Alexander, S. R., Aruna, S. T. R., "Combustion synthesis in nanostructured reactive systems," *Adv. Powder Technol.*, vol. 26, pp. 954-976, 2015.
- [53] Nazari, A., Riahi, S., "Sadhana-Acad". *Proc. Eng. Sci.* vol. 36, pp. 371–391, 2011.
- [54] Patil, K.C., Hegde, M.S., Rattan, T., Aruna, S.T., "Chemistry of Nanocrystalline Oxide Materials, Combustion Synthesis, Properties and Applications". *World Scientific*, vol. 46, pp. 274-278, 2008.
- [55] Ekambaram, S., Patil, K.C., Maaza, M., "Synthesis of lamp phosphors: facile combustion approach". *J. Alloys Compd.* Vol. 393, pp. 81–92, 2005.
- [56] Kingsley, J.J., Patil, K.C., "A novel combustion process for the synthesis of fine particle α -alumina and related oxide materials". *Material Letter*, vol. 6 pp. 427–432, 1988.
- [57] Aruna, S.T., Mukasyan, A.S., "Combustion synthesis and nanomaterials". *Curr. Opin. Solid St. M.* vol. 12, pp. 44–50, 2008.
- [58] Patil, K.C., Aruna, S.T., Mimani, T., "Combustion synthesis: an update". *Curr. Opin. Solid St. M.* vol. 6, pp. 507–512, 2002.
- [59] Patil, K.C., Aruna, S.T., Ekambaram, E., "Combustion synthesis". *Curr. Opin. Solid St. M.* vol. 2, pp. 158–165, 1997.

- [60] Ianoş, R., Lazău, I., Păcurariu, C., “The influence of combustion synthesis conditions on the α -Al₂O₃ powder preparation”. *J. Mater. Sci.* vol. 44, pp. 1016–1023, 2009.
- [61] Jadhav, L.D., Patil, S.P., Chavan, A.U., Jamale, A.P., Puri, V.R., “Solution combustion synthesis of Cu nanoparticles: a role of oxidant-to-fuel ratio”. *Micro & Nano Letters*, vol. 6, pp. 812–815, 2011.
- [62] Huang, H.H., Yan, F.Q., Kek, Y.M., Chew, C.H., Xu, G.Q., Xi, W., Oh, P.S. and Tang, S.H., “Synthesis, characterization, and nonlinear optical properties of copper nanoparticles”. *Langmuir*, vol. 13, pp. 172–175, 1997.
- [63] Zhou, F., Zhou, R., Hao, X., Wu, X., Raw, W., Chen, Y., Gao, D., “Influences of surfactant (PVA) concentration and pH on the preparation of copper nanoparticles by electron beam irradiation”. *Radiation Physics and Chemistry*, Vol. 77, pp. 169–173, 2008.
- [64] Rafael, M., Yitzhak, M., Silvia, G., Katharina, L., "Colloidal systems for crystallization processes from liquid phase," *RSC Adv.*, vol. 15, pp. 2175–2191, 2013.
- [65] Khan, M., Ansari, S., Ansari, O., Min, B., Lee, J., “Biogenic fabrication of AuCeO₂ nanocomposite with enhanced visible light activity”. *J Phys Chem*, vol. 118, pp. 9477–9484, 2014.
- [66] Fujishima, A., Honda, K., “Electrochemical photolysis of water at a semiconductor electrode”. *Nature*, vol. 238(5358), pp. 37–38, 1972.
- [67] Rajeshwar, K., Osugi, E., Chanmanee, W., Chenthamarakshan, C., Zaroni, M., Kajitvichyanukul, P., Krishnan-Ayer, R., “Heterogeneous phot catalytic treatment of organic dyes in air and aqueous media”. *J. Photochem Photobiol*, vol. 9(4), pp. 171–192, 2008.
- [68] Saravanan, R., Karthikeyan, S., Gupta, V.K., Sekaran, G., Narayanan, V., Stephen, A., “Enhanced photocatalytic activity of ZnO/CuO nanocomposite for the degradation of textile dye on visible light illumination”. *Mater Sci Eng C Mater Biol Appl*. Vol. 33(1), pp. 91–98, 2013.
- [69] Gnanasekaran, L., Hemamalini, R., Ravichandran, K., “Synthesis and characterization of TiO₂ quantum dots for photocatalytic application”. *J Saudi Chem Soc*. Vol. 19(5) pp. 589–594, 2015.

- [70] Saravanan, R., Thirumal, E., Gupta, V.K., Narayanan, V., Stephen, A., “The photocatalytic activity of ZnO prepared by simple thermal decomposition method at various temperatures”. *J Mol Liq*, Vol. 177, pp. 394–401, 2013.
- [71] Cullity, B.D., Stock, S.R., “Book name-Elements of X-Ray diffraction, Prentice-Hall”. 2001.
- [72] Biswas, M., “Growth and Characterisation of ZnO Nanostructures”. Excitonic Properties and Morphology”. Vol. 362, pp. 142-147, 2010.
- [73] Ugemann, L.B., “Nuclear Instruments and Methods in Physics Research”. Vol. 531, pp. 292–301, 2004.
- [74] Chattergy, S., Roy, A., Lasker, A., Swarnaker, S., “Electron Microscopy in the perspective of modern Biology: Ultravision and Ultradimension”. *JOM*, vol. 47 (9), pp. 13-17, 1995.
- [75] Bykov, I., “Characterization of Natural and Technical Lignins using FTIR Spectroscopy”. Luleå University of Technology, 2008.
- [76] Swann, G. E.A., Patwardhan, S.V., “Application of fourier transformed infrared spectroscopy (FTIR) for assessing biogenic silica sample purity in geochemical analyses and palaeo environmental research, Climate of the past”. Vol. 7, pp. 65-74, 2011.
- [77] Movasaghi, Z., Rehman, S., Rehman, I.U., “Fourier Transform Infrared (FTIR) Spectroscopy of biological Tissue”. *App. Spectroscopy Rev.*, Vol. 43, pp. 134–179, 2008.
- [78] Bouazizi, N., Bargougui, R., Queslati, A., Benslama, R., “Effect of synthesis time on structural, optical and electrical properties of CuO nanoparticles synthesized by reflux condensation method”. *Adv.Mater. Letters*, vol. 6, pp. 158-164, 2015.
- [79] Chaudhary, S., Sharma, P., Kumar, R., Metha, S.K., “Nanoscale surface designing of Cerium Oxide nanoparticles for controlling growth, stability, optical and thermal properties”. *Ceramic Int.*, vol. 41, pp. 10995– 11003, 2015.
- [80] Omar, H., Elkader, A., and Deraz, N.M., “Synthesis and Characterization of New Copper based Nanocomposite”. *Int. J. Electrochem. Sci.*, vol.8 pp. 8614 – 8622, 2013

- [81] Scrivener K.L., Fulmanna T, Galluccia, G. Walentab G, Bermejo G.E.: Quantitative study of Portland cement hydration by X-ray diffraction/Rietveld analysis and independent methods, *Cement and Concrete Research*, Vol. 34, pp. 1541–1547, 2004.
- [82] Rodríguez J, Carvajal, “How to work with symmetry modes using FullProf and AMPLIMODES”. Institut Laue-Langevin, 6 rue Jules Horowitz, BP Vol. 156, pp. 274-284. 2008.
- [83] Izumi F, Momma K, “Three-dimensional Visualization in Powder Diffraction”. *Solid State Phenomena*, Vol. 130, pp 15-20, 2007.
- [84] Brian, H., Toby, B., H, “R factors in Rietveld analysis: How is good enough”? *Powder Diffraction* 21 (1), March 2006
- [85] Kannadasan, N., Shanmugam, N., Cholan, S., Sathishkumar, K., Viruthagiri, G., and Poonguzhali, R., *Mater. Charact.* Vol. 97, pp. 37–46, 2014.
- [86] Ren, G., Hu, D., Cheng, E.W.C., Vargas-Reus, M.A., Reip, P., Allaker, R.P., “Characterization of copper oxide nanoparticles for antimicrobial applications”. *Int. J. Anti. Agent.*, vol. 33, pp. 587- 590, 2009.
- [87] Huang, H.H., Yan, F.Q., Kek, Y.M., Chew, C.H., Xu, G.Q., Xi, W., Oh, P.S. and Tang, S.H., “Synthesis, characterization, and nonlinear optical properties of copper nanoparticles”. *Langmuir*, vol. 13, pp. 172–175, 1997.
- [88] Siddiqui, H., Qureshi, MS., Haque, F.Z., “Hexamine (HMT) assisted wet chemically synthesized CuO nanostructures with controlled morphology and adjustable optical behavior”. *Opt Quantum Electron*, vol. 48, pp. 349–364, 2016.

END